



Master thesis

# Thin targets in extreme conditions: probing high-brightness hadron beams

Manon BOUCARD

Supervisor: Dr. Mariusz SAPINSKI

Responsible: Prof. Dr. Mike SEIDEL

External expert: Dr. Federico RONCAROLO

*A thesis submitted in partial fulfilment of the requirements for the degree of  
Master of Science MSc in Applied Physics*

*In the*  
**Particle Accelerator Physics Laboratory**  
**École polytechnique fédérale de Lausanne**

*Master project realised at*  
**Paul Scherrer Institut**

**PAUL SCHERRER INSTITUT**



1st September 2023



# Acknowledgements

Firstly, I'd like to warmly thank Dr. Mariusz Sapinski, my supervisor, who accompanied and guided me throughout this project. His enthusiasm, motivation, and knowledge have enabled me to learn a lot and discover a part of the world of beam instrumentation. Thanks for your confidence.

I'd like to thank my responsible teacher, Prof. Dr. Mike Seidel, for giving me the chance to do this project and for doing everything he could to make it happen in the best possible conditions.

I would also like to thank Dr. Tatiana Pieloni, who has supported me since I joined the LPAP, answering all my questions and helping me a lot. Thank you for everything.

I also thank Dr. Federico Roncarolo for having accepted to be the external expert for this work.

I would like to thank Dr. Rudolf Dölling for his wise advice and for inspiring the subject of this thesis.

I thank Dr. Elisabeth Müller for the electron microscope analysis.

I would also like to thank all the people with whom I had the opportunity to talk during my time at PSI and who provided me with answers when I had questions.

I thank Dr. Araceli Navarro and Dr. Dominik Vilsmeier for the time they spent helping me to understand their respective codes.

Enfin je souhaite remercier chaleureusement tous mes amis, celles de toujours, qui me connaissent par cœur et qui m'aiment quand même, et ceux de Lausanne, qui ont vécu avec moi tous les bons et les mauvais moments que nous a donné à vivre l'EPFL. Mais surtout, je remercie du fond du cœur ma famille, Papa, Maman, Sam et Lilou, merci de m'avoir permis d'être là où j'en suis, de m'encourager au quotidien, de me soutenir, et de me donner tout votre amour, je vous aime fort.

Manon Boucard



# Abstract

Thin targets used in beam instrumentation for high-brightness hadrons beams are subject to extreme conditions. Those of wire scanners see their temperature rise very quickly due to the passage of the beam. In addition to the secondary electron current used to measure the transverse profile of the beam, this temperature increase will cause the emission of thermionic electrons that will distort the measured signal. At Paul Scherrer Institut (PSI), in the proton accelerator (HIPA for High-Intensity Proton Accelerator), to suppress these thermionic emissions a bias voltage is applied to the wire of the probe called RRL. This work shows that this bias voltage is not sufficient to totally suppress the thermionic electrons in the case of HIPA. This could be due to the effect of the bunch potential. This thesis then aims to find solutions for the suppression of thermionic emission. For this purpose, a simulation code called PyTT based on the finite element method which simulates the temperature and the signal emitted by the wire scanner is experimentally benchmarked. This benchmarking shows that the code has a high sensitivity to certain wire material properties. PyTT simulations are done to show that if the diameter of the wire is reduced then the thermionic emission could be suppressed. A decrease of about 76 % of the wire diameter (from  $34 \mu\text{m}$  to  $8 \mu\text{m}$ ) could suppress all the thermionic current even with the highest beam current reached at HIPA (2.5 mA). However, a wire that is too thin can be mechanically weaker and difficult to be installed. Thanks to the PyTT code, a simulation series is done to compare the thermal evolution of the wire with various materials: carbon fibre wire, which is used now in RRL, and carbon nanotube wires, a very promising low-density material. Results show that using low-density materials decreases the temperature reached by the target and then reduces thermionic emission and even could suppress them without using a bias voltage or ultra-thin wire.



# Résumé

Lorsqu'un faisceau de particule circule dans un accélérateur il est impossible de l'observer à l'œil nu. Pour cette raison, plusieurs appareils permettant de mesurer l'énergie, l'intensité, la taille, les profiles transverses et le profil longitudinal ou encore les pertes d'un faisceau sont placés le long de sa trajectoire. On appelle l'ensemble de ces appareils l'instrumentation faisceau.

Ce travail se concentre sur un de ces instruments en particulier, le scanner à fil. Il permet de déterminer le profil transverse du faisceau de particules. Un fil, souvent fait de fibre de carbone, de molybdène ou de tungstène, est déplacé à vitesse constante à travers le faisceau. L'interaction entre le fil et le faisceau produit des particules secondaires dont l'émission est proportionnelle à la densité de particules. Certains scanners se basent sur la mesure du courant généré par les électrons secondaires alors que d'autres détectent les particules de haute énergie produites par l'interaction.

A l'Institut Paul Scherrer (PSI) situé dans le canton d'Argovie en Suisse, l'accélérateur de proton HIPA (High Intensity Proton Accelerator) est doté d'un scanner à fil nommé RRL. Cette sonde mesure le courant généré par l'émission des particules secondaires et permet de scanner toutes les orbites empruntées par le faisceau. Un des problèmes majeurs de ce type de sonde est que, lorsque l'intensité du faisceau augmente, la température du fil augmente aussi et mène à l'émission d'électrons dits thermoïoniques. Ce sont des électrons qui ont acquis suffisamment d'énergie thermique pour s'échapper du fil. Cependant cette émission va déformer le profil produit par les électrons secondaires et perturber la mesure. Pour la supprimer, la solution mise en place à ce jour est d'appliquer une tension de polarisation au fil.

La première partie de ce travail a pour but d'observer l'influence de cette tension de polarisation sur la mesure du profil transverse en utilisant des mesures faites par RRL en 2022. Ces mesures montrent que cette solution n'est pas suffisante car on observe une émission résiduelle d'électrons thermoïoniques à hauteur de 8 %. Ce courant restant pourrait être dû aux effets du potentiel du faisceau.

La suite de ce travail se focalise sur la recherche de solutions pour supprimer cette émission thermoïonique. Pour cela, un code basé sur la méthode des éléments finis, PyTT, est utilisé. Premièrement il est mis à l'épreuve en comparant des résultats de simulation avec les mesures effectuées par RRL. Cette comparaison permet de mettre en avant la fiabilité du code pour reproduire des profiles avec des courants thermoïoniques modérés. Il montre aussi une grande sensibilité à certaines propriétés du matériau composant le fil, comme la fonction de travail et l'émissivité.

Ce code permet d'étudier comment le diamètre de fil influence les émissions thermoïoniques. Les simulations montrent qu'un fil de  $8 \mu\text{m}$  de diamètre permettrait

d'éliminer toutes les émissions thermoïoniques, et cela pour des faisceaux de courant allant jusqu'à 2.4 mA, le plus grand courant obtenu dans HIPA. Cependant, ces fils ultra fins sont plus faibles et sont difficiles à installer.

La dernière partie considère l'utilisation de cibles faites en matériaux de faible densité pour remplacer les matériaux utilisés actuellement. L'évolution thermique des fils en fibre de carbone (matériau actuel) est comparée à celle de fils en nanotube de carbone (matériau de faible densité). D'après ces simulations, les émissions thermoïoniques seraient totalement supprimées dans le cas des faisceaux sondés par RRL au PSI en utilisant des fils en nanotubes de carbone sans avoir recours à une tension de polarisation ou des fils ultrafins.

# Contents

<b>1</b>	<b>Introduction</b>	<b>10</b>
<b>2</b>	<b>PSI and HIPA presentation</b>	<b>12</b>
2.1	PSI in brief . . . . .	12
2.2	The proton accelerator facility HIPA . . . . .	13
2.2.1	The main components of HIPA . . . . .	13
2.2.2	Proton beam applications . . . . .	14
2.3	Kinetic energy of beam in cyclotron . . . . .	15
<b>3</b>	<b>Beam instrumentation</b>	<b>16</b>
3.1	Beam transverse profile measurements: wire scanners . . . . .	16
3.2	PSI's Main Ring Cyclotron Radial Probe (RRL) . . . . .	17
<b>4</b>	<b>Interaction between the wire and the beam</b>	<b>20</b>
4.1	The energy deposition . . . . .	20
4.2	Wire heating model . . . . .	21
4.3	Wire signal: Secondary Emission and Thermionic Emission currents .	23
4.3.1	The energy distribution of secondary and thermionic electrons	25
4.4	Thermionic peak . . . . .	26
<b>5</b>	<b>Observation of the influence of bias voltage on the wire signal</b>	<b>28</b>
5.1	Application of the bias voltage . . . . .	28
5.2	Discussion . . . . .	31
<b>6</b>	<b>Simulations with PyTT</b>	<b>34</b>
6.1	Parameters . . . . .	34
6.1.1	Beam parameters . . . . .	34
6.1.2	Wire parameters . . . . .	37
6.1.3	Wire's material parameters . . . . .	37
6.1.4	Other parameters . . . . .	38
6.2	Benchmarking . . . . .	39
6.2.1	Presentation of the three chosen cases . . . . .	39
6.2.2	Results of the simulations . . . . .	40
6.2.3	Comparison with measurements and discussion . . . . .	42
6.2.4	Wire signal's high sensitivity on work function and emissivity	43
6.3	Wire diameter study . . . . .	45

<i>CONTENTS</i>	9
-----------------	---

<b>7 Low-density materials as wire scanners target</b>	<b>48</b>
7.1 Materials parameters . . . . .	48
7.2 Beam parameters . . . . .	50
7.3 Wire parameters . . . . .	51
7.4 Simulations parameters . . . . .	51
7.5 Results of the simulations and discussion . . . . .	52
7.5.1 Thermal behaviour . . . . .	52
7.5.2 Wire damage due to contamination . . . . .	55
7.5.3 Wire signal . . . . .	57
<b>8 Conclusions and perspectives</b>	<b>60</b>

# Chapter 1

## Introduction

When a beam of particles travels through an accelerator, it is impossible to directly observe what is happening with our own eyes. However, we need to know exactly what is happening inside so that, for example, we can stop the beam from damaging the machines due to abnormal behaviour. To observe the beam, instruments capable of measuring certain parameters need to be put in place. The art of measuring beam parameters is called beam instrumentation or beam diagnostic [1]. Those instruments are the eyes of the machine. They are placed at strategic points in the accelerator, and measure several beam parameters such as energy, current, size, beam transverse profiles, bunch longitudinal profile and losses. Depending on the energy range of the beam or the type of particle it contains, the instruments used to measure the same parameter will not be the same.

In this report, we will focus on the measurement of the beam's transverse profile, and more specifically on one of the main instruments used to observe it: wire scanners [2]. This is an instrument with a wire, often made of carbon fibre, molybdenum, or tungsten, which is moved at a constant speed through the beam. The interaction between the wire and the beam produces secondary particle emissions. Depending on the type of wire scanner, either the current produced by secondary electrons is measured or a shower of high-energy particles, produced in nuclear interactions, is detected.

At PSI (Paul Scherrer Institut) [3], a Swiss multidisciplinary research laboratory, this instrument is used to measure the transverse profile of a proton beam accelerated by HIPA (High-Intensity Proton Accelerator), a complex of cyclotrons providing one of the most powerful particle beams in the world [4]. There are almost 100 wire scanners in HIPA, but we will only look at one of them: the long radial probe RRL. This is the most advanced probe and the newest one (commissioning in 2022 [5]) allowing us to measure beam profile at all intensities.

The measurement of the transverse profile is based on the measurement of the current produced by the secondary electron emission, which is proportional to the particle density in the beam. However, when the beam current increases, the wire temperature also increases and another electron emission phenomenon comes into play: thermionic emission [6]. This emission is due to electrons in the wire acquiring enough thermal energy to escape. This current disturbs the profile measurement and must be suppressed. To reduce this thermionic emission, one solution is to apply a

bias voltage to the wire.

The aim of this thesis is to study the efficiency of the bias voltage on the thermionic emission and its influence on the measurement of the beam transverse profile. Another objective is to simulate the thermal evolution of the wire using a finite element code, whose experimental benchmarking is an integral part of this work. Those simulations are used to understand how by changing the wire properties (in this work: the wire diameter and the wire material), the probe could be more efficient.

After an introduction to PSI and HIPA (Chapter 2) and a more detailed presentation of how RRL works (Chapter 3), Chapter 4 will be devoted to the interactions between the beam and the wire, in particular the model that describes the heating of the wire and the currents generated. This will be followed by Chapter 5 on the influence of bias voltage on signal measurement. After that, a simulation program (PyTT [7]), which calculates the maximum temperature reached by the wire as well as the currents produced during the passage of a beam, will be presented and benchmarked (Chapter 6). In the same Chapter, simulations with this code are done to determine how the thermionic emission peak evolves with the size of the wire. Finally, Chapter 7 will focus on the study of new low-density materials, to replace the materials currently used, in order to increase the performance of the instruments.

# Chapter 2

## PSI and HIPA presentation

### 2.1 PSI in brief

Paul Scherrer Institut (PSI) is the biggest research centre in Switzerland for natural and engineering sciences [3]. It was created in 1988 with the merger of the Swiss Federal Institute for Reactor Research and the Swiss Institute for Nuclear Research. Located in the canton of Aargau (in the municipalities of Villigen and Würenlingen) it is a multi-disciplinary research institute focusing on four main areas of research: future technologies, energy and climate, health innovation, and fundamental research (see Figure 2.1).



Figure 2.1: Aerial view of the PSI facilities. (Courtesy of Mariusz Sapinski)

PSI has several large research facilities such as:

- HIPA (High-Intensity Proton Accelerator), which will be described more in detail in the next Section.

- A proton therapy system (Proscan) fed by COMET (Compact Medical Cyclotron) cyclotron, which can treat deep-seated tumours with two gantries of different types and eyes tumours with Optis2 beamline [8].
- The Swiss Light Source (SLS), is a third-generation synchrotron light source. Thanks to the high-brightness and broad spectrum of the photon beam, research in material sciences, biology, and chemistry can be done and the detailed composition of the smallest structure down to nanometer size can be determined [9].
- The free-electron laser SwissFEL is an X-ray free-electron laser that produces extremely short and intense flashes of X-ray radiation of laser quality. This allows for the observation of extremely quick processes and the production of films showing the motion of atoms and molecules [10].

## 2.2 The proton accelerator facility HIPA

The proton accelerator facility is made up of a series of accelerators and is considered to be a high-performance proton accelerator, its name is HIPA (for High-Intensity Proton Accelerator) [4], [11]–[13]. Currently, it produces the highest-power particle beam in Europe.

### 2.2.1 The main components of HIPA

**1) The proton source** The first step is the proton source, hydrogen gas is irradiated with micro-waves to remove electrons and leave only the atomic nuclei composed of one proton [12]. The source used in PSI is based on Electron Cyclotron Resonance (ECR) phenomena, in which electrons in the source chamber move in circular orbits colliding with many atoms. This type of source allows for high-intensity of ion beams. Protons leave the source with a 60 keV kinetic energy.

**2) The Cockcroft and Walton DC acceleration** These protons are submitted to an electrostatic field accelerating them by 810 keV by the Cockcroft and Walton linear accelerator (see Figure 2.2), the final protons' kinetic energy is 870 keV and they reach a speed of almost 4 % of the speed of light [12].



Figure 2.2: Cockcroft and Walton DC accelerator [12] (Photo: Paul Scherrer Institute)

**3) Injector 2** Next, the protons are guided towards Injector 2 (see Figure 2.3), which is an isochronous cyclotron: four resonators produce an alternating electromagnetic field (with 50 MHz frequency) that accelerates the protons, and four magnets bend the trajectory of the proton beam so that it follows orbits [13]. At the end of the 80 orbits, the protons have an energy of 72 MeV (38 % of the speed of light).

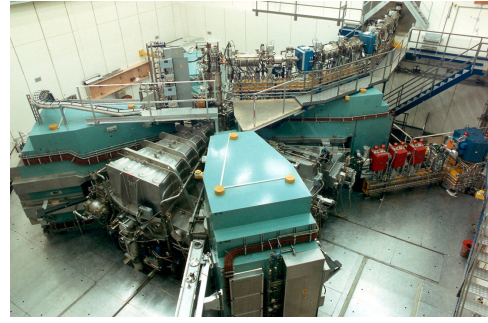


Figure 2.3: Injector-2 cyclotron [13]  
(Photo: Paul Scherrer Institute)

**4) Main Ring Cyclotron** Finally, these protons are injected into the Ring Cyclotron (see Figure 2.4). This is called a ring because the energy at injection is already 72 MeV, so the first orbits are already quite large, with a radius of 2048 mm. As Injector 2, this is also an isochronous cyclotron equipped with four resonators at 50 MHz [11]. A fifth cavity, 150 MHz, is added to increase the number of extracted particles. There are 8 sector magnets. The extraction energy is 590 MeV (80 % of the speed of light) after about 186 orbits (4 km long track) with an outer radius of 4480 mm. The maximum beam current is 2.4 mA, making HIPA one of the world's most powerful continuous beam particle accelerators with 1.4 MW beam power [4]. Inside the accelerators, protons travel in bunches of a few millimetres in size.



Figure 2.4: Main Ring cyclotron [4]  
(Photo: Paul Scherrer Institute)

### 2.2.2 Proton beam applications

The proton beam is used for three different applications (see Figure 2.5):

- The muon source ( $S\mu S$ ): the proton beam hits a carbon graphite target, which produces a polarized muon beam. This muon beam is mainly used to determine magnetic fields in the material interior and for research on positive muon or muonium [14].
- The spallation neutron source (SINQ): the proton beam strikes a lead target and knocks the neutrons out of the lead nuclei. These neutrons can be used to study new materials like superconductors or computer materials. They can also be used for neutron radiography and tomography [15].

- An ultracold neutron source (UCN): the proton beam is directed to strike a lead target. The neutrons produced by spallation are thermalized in water and then passed into a vessel containing solid deuterium at a temperature of 5 K to become Ultra Cold Neutrons. UCNs are useful tools to study the properties of neutrons and especially the search for a permanent electric dipole moment [16].

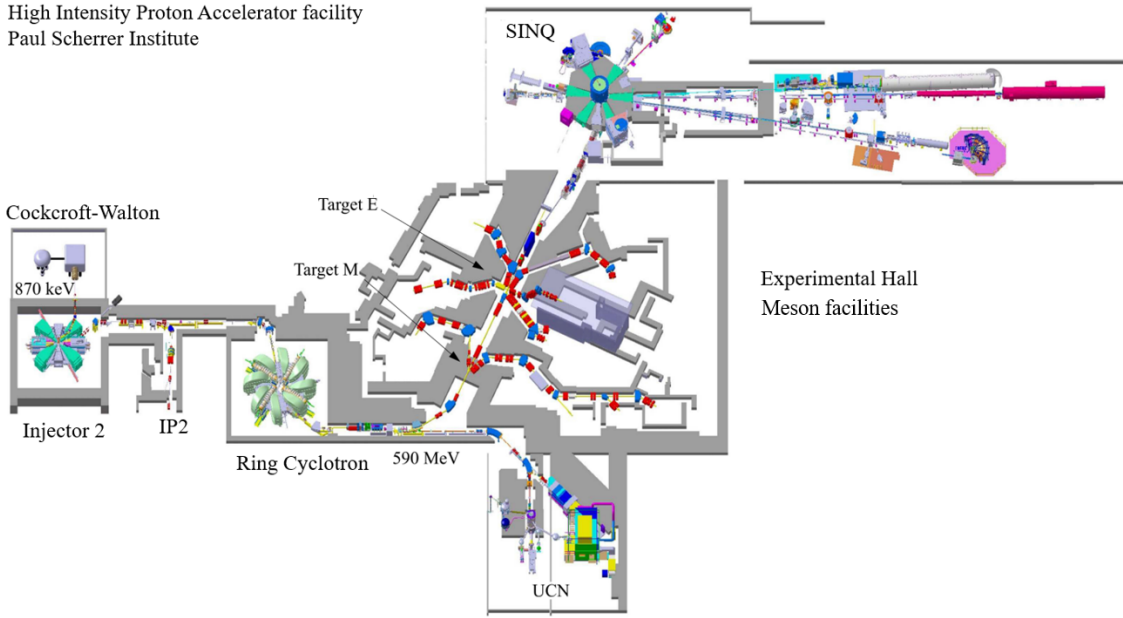


Figure 2.5: Layout of the High-Intensity Proton Accelerator facility at the Paul Scherrer Institute. (Courtesy of Joachim Grillenberger / Paul Scherrer Institute, from [11])

### 2.3 Kinetic energy of beam in cyclotron

To find out the kinetic energy of the beam travelling in a given orbit of a cyclotron, one has to use the fact that in each resonator, the beam gains kinetic energy of approximately 0.84 MeV. So, to find the energy of the beam at orbit  $n$ ,  $E_n$ , the following formula applies:

$$E_n = E_0 + (n - 1) \cdot 4 \cdot 0.84 \quad (2.1)$$

where  $E_0$  is the injection energy which is 72 MeV for the Main Ring Cyclotron. The formula (2.1) is approximate, because the electric field in the cavity has a sinusoidal shape, so the acceleration amplitude is smaller at initial and final orbits. In addition, the fifth cavity working at 150 MHz and used to increase longitudinal acceptance of the machine also affects the accelerating field. The particles are accelerated over approximately 186 turns (called also orbits) to reach an energy of 590 MeV.

# Chapter 3

## Beam instrumentation

Beam diagnostics and instrumentation are used to measure beam parameters in particle accelerators [2]. Different instruments can measure different parameters such as beam position, beam current, beam transverse and longitudinal profiles, tune, emittance and beam losses

### 3.1 Beam transverse profile measurements: wire scanners

The transverse beam profile is one of the most important beam parameters and is measured in almost all accelerators using various techniques. Among the most commonly used instruments is the wire scanner [2].

Wire scanners probe the transverse beam density by moving a thin target (which is usually a wire, hence the name) through the beam and measuring the effects of the interaction. The wires are very thin, therefore they are typically mounted on a fork or another moving support. Scanners can be classified as linear or rotational, depending on the wire trajectory. Rotational devices can reach very high speeds (up to  $20 \text{ m s}^{-1}$ ), while linear devices are slower but usually more precise. Wires are usually made from carbon fibres, tungsten, or molybdenum but new materials, such as low-density materials are under study to be used as thin targets, properties of these materials are put in Table 3.1.

	Density [ $\text{g cm}^{-3}$ ]	Melting Temperature [K]	Z
Carbon fibre	2.1	3915	6
Carbon Nanotube	1.0-0.2	3915	6
Molybdenum	10.3	2896	42
Tungsten	19.3	3695	74

Table 3.1: Properties of thin target materials [17]. For carbon fibre and carbon nanotube, the sublimation temperature is written instead of the melting temperature because carbon can melt only at very high pressures.

For low beam energies, the wire scanners are interceptive devices, i.e. the beam particles are stopped or strongly scattered by the wire. At high energies the beam disturbance is negligible, however, measurement generates a beam loss, which, in

cases of high-intensity machines, may be potentially harmful. Therefore the scans are usually done relatively rarely and 'on demand'.

Depending on the beam energy, two types of measurements can be done [2], [18]:

- If the beam energy is relatively small, the profile is reconstructed using the current generated by the interaction between the beam and the wire.
- If the beam energy is higher, the beam profile is reconstructed by detecting, usually using scintillators and photo-multipliers, the high-energy secondary particles emitted when the wire interacts with the beam. The secondary particles must have enough energy to cross the vacuum chamber wall (5 mm of aluminium) and still give signal in scintillators.

### 3.2 PSI's Main Ring Cyclotron Radial Probe (RRL)

For the PSI's Main Ring Cyclotron the transverse beam profile is measured using the Long Radial Probe, called RRL [5]. This wire scanner can scan all the orbits along the ring cyclotron radius,  $\approx 2.5$  m (from the inner radius of 2.048 m to the outer radius of 4.480 m). At the minimum beam energy of 72 MeV (energy at injection) not many high-energy secondary particles are generated, therefore the profile is reconstructed with the wire current.

RRL is made up of 3 wires, a vertical and two tilted (with  $\pm 45^\circ$  angle) (see Figure 3.1). The three wires are used to measure the horizontal and diagonal profiles and with a few manipulations (see Section 6.1.1) it is possible to obtain the vertical profile. They are made from carbon fibres and have a diameter of  $34\ \mu\text{m}$ . They are mounted on trolleys that move synchronously thanks to the same stepper motor and two identical drive mechanisms. The speed of the trolleys is  $29.7\ \text{mm s}^{-1}$ . Figure 3.2 shows the complete structure of RRL. On the left, there is a structure that can be placed in or removed from the cyclotron allowing for service without breaking the cyclotron vacuum. The location of RRL in the cyclotron is shown in Figure 3.3.

Signals from the wires are read out by MESON module which comprises logarithmic current amplifiers and digitizes the signal with a 2 kHz rate. The electronics are placed outside of the cyclotron bunker and the cables have a length of about 86 m.

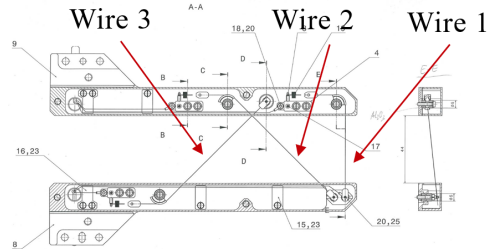


Figure 3.1: Schema of the three wires mounted on two trolleys moving synchronously (Courtesy of Martin Rohrer / Paul Scherrer Institute).

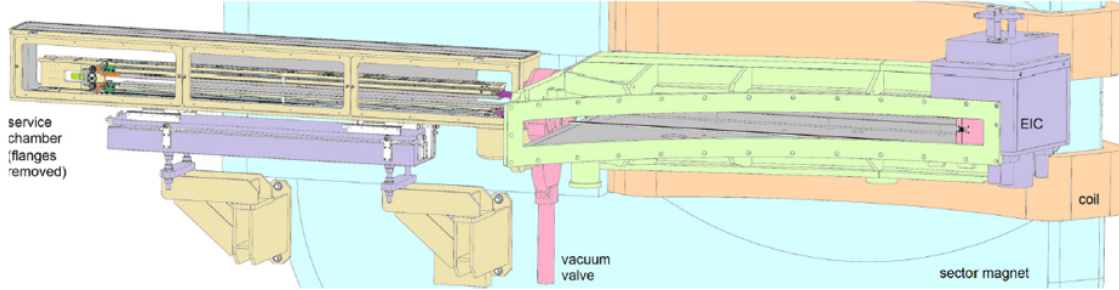


Figure 3.2: RRL structure (Courtesy of Martin Rohrer / Paul Scherrer Institute).

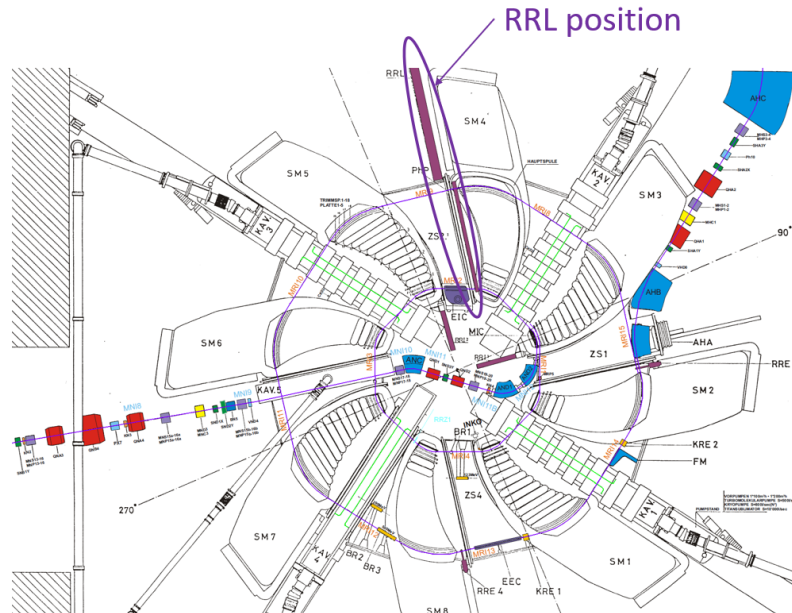


Figure 3.3: Top view of the Main Ring Cyclotron with RRL position (Technical drawing: Paul Scherrer Institute).

An entire scan can be seen in Figure 3.4. The signal of the three wires is represented by different colours. Wire 1 (the vertical one) scans every orbit, wire 2 skips the first one and wire 3 skips the 3 first ones. Because of the 2 kHz readout, the scan contains about 160000 data points, per wire and per direction. Figure 3.5 shows a zoom of the profile to see more clearly the three wire signals. The signals from the tilted wires are larger than that from the horizontal wires. This is because, even though the wires are moving at the same speed as all 3 are attached to the same trolleys, the tilted wires remain in contact with the beam for longer, due to the fact that they do not take the shortest path. This difference is a factor of  $\sqrt{2}$ , which is due to the 45° inclination of the wires. During each scan, the trolleys move from the most outside position to the machine centre (scan IN) and back (scan OUT).

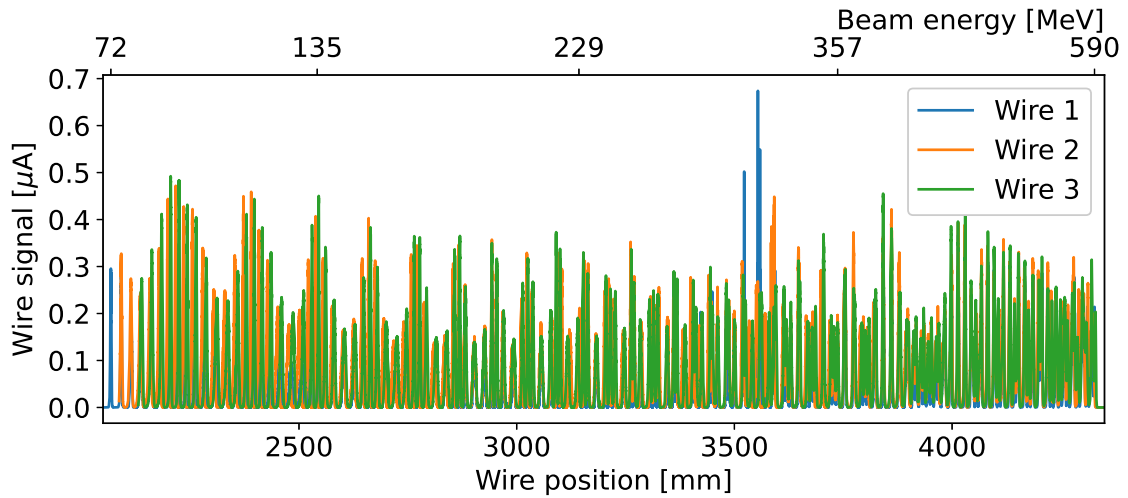


Figure 3.4: Scan IN of the full profile for  $413 \mu\text{A}$  beam current, with the 186 orbits, for the three wires.

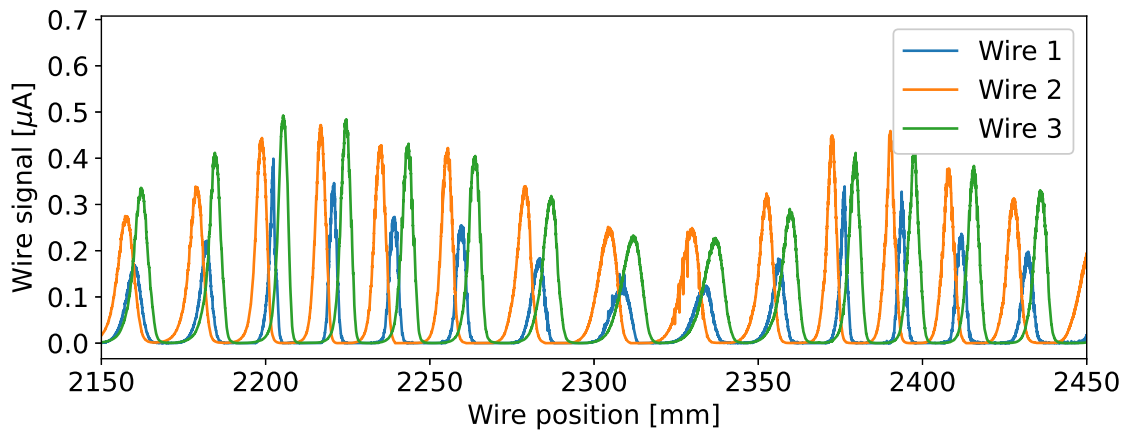


Figure 3.5: Zoom of the full scan from Figure 3.4 for  $413 \mu\text{A}$  beam current, between 2150 mm and 2450 mm, for the three wires. 14 orbits are visualized.

# Chapter 4

## Interaction between the wire and the beam

### 4.1 The energy deposition

When a charged particle crosses through matter it mainly interacts with the electrons losing its energy. This energy loss depends on the type of particle, the beam energy, and the target material. A practical way to describe the amount of lost energy is using the concept of stopping power, which is the energy lost per length of particle track in the material normalised to material density. For heavy particles, like protons, it is calculated using the Bethe-Bloch formula [19]:

$$\left\langle -\frac{dE}{dX} \right\rangle = K z^2 \frac{Z}{A} \frac{1}{\beta^2} \left[ \frac{1}{2} \ln \frac{2m_e c^2 \beta^2 \gamma^2 W_{\max}}{I^2} - \beta^2 - \frac{\delta(\beta\gamma)}{2} \right] \quad (4.1)$$

which depends on  $z$  the charge of the incident particle,  $Z$  the charge number of the medium,  $A$  [g mol<sup>-1</sup>] the atomic mass of the medium,  $I$  [eV] the mean excitation energy of medium,  $\delta$  the density correction, the relativistic  $\beta$  and  $\gamma$  the Lorentz factor.  $m_e = 511$  keV  $c^{-2}$  is the electron mass,  $K = 4\pi N_A r_e^2 m_e c^2 = 0.307$  MeV cm<sup>2</sup> mol<sup>-1</sup> ( $N_A = 6.022 \cdot 10^{23}$  mol<sup>-1</sup> the Avogadro's number and  $r_e = 2.8$  fm the classical electron radius) and  $W_{\max} = \frac{2m_e c^2 \beta^2 \gamma^2}{1+2\gamma m_e/M+(m_e/M)^2}$  eV the maximum energy transfer in single collision ( $M$  [eV  $c^{-2}$ ] the mass of the incident particles). The units of the stopping power is [MeV cm<sup>2</sup> g<sup>-1</sup>]. The stopping power is sometimes confused with linear energy transfer (LET), which is not normalised to material density and has units of [MeV cm<sup>-1</sup>].

Usually, most of the energy lost by the particle is deposited in the material and can be considered as a heat inflow. However, for very thin targets, as in the case of carbon fibre, some of the electrons that gain high energy interacting with the beam particles (so-called  $\delta$ -electrons) escape carrying out a significant fraction of the energy foreseen by Bethe-Bloch equation [20]. Those  $\delta$ -electrons are not taken into account in the calculation of the stopping power in this work.

## 4.2 Wire heating model

As written before, when the beam or protons passes through the wire it deposits energy. This deposition of energy leads to a temperature increase of the wire. However, cooling processes come also into play rapidly due to the small size of the wire. The thermal evolution of the wire is described by M. Sapinski [21] and the following formulations are based on the PhD thesis of A. Navarro [18]. The temperature evolution is described with the heat equation:

$$\left(\frac{\partial T}{\partial t}\right)_{\text{Tot}} = \left(\frac{\partial T}{\partial t}\right)_{\text{BH}} - \left(\frac{\partial T}{\partial t}\right)_{\text{RC}} - \left(\frac{\partial T}{\partial t}\right)_{\text{CC}} - \left(\frac{\partial T}{\partial t}\right)_{\text{TC}} \quad (4.2)$$

with  $\left(\frac{\partial T}{\partial t}\right)_{\text{BH}}$  the beam heating,  $\left(\frac{\partial T}{\partial t}\right)_{\text{RC}}$  the radiative cooling,  $\left(\frac{\partial T}{\partial t}\right)_{\text{CC}}$  the conduction cooling,  $\left(\frac{\partial T}{\partial t}\right)_{\text{TC}}$  the thermionic cooling.

**Beam heating:** Caused by the direct beam energy deposition, the thermal evolution due to the beam heating can be expressed as follows:

$$\left(\frac{\partial T}{\partial t}\right)_{\text{BH}} = \frac{\Phi(x, y, t) \cdot S_{CS}}{\rho \cdot C_p(T) \cdot V} \cdot \frac{\pi}{4} d \frac{dE}{dx} \rho \quad (4.3)$$

with  $\Phi(x, y, t)$  [ $\text{cm}^{-2} \text{s}^{-1}$ ] the flux of incoming particles,  $S_{CS}$  the cross-sectional surface (drawn on Figure 4.1),  $d$  the diameter of the wire,  $\rho$  [ $\text{g cm}^{-3}$ ] the density of the material,  $C_p(T)$  [ $\text{J g}^{-1} \text{K}^{-1}$ ] the heat capacity of the wire,  $V$  the volume taken into account and  $\frac{dE}{dx}$  [ $\text{MeV cm}^2 \text{g}^{-1}$ ] the stopping power discussed before ( $\frac{\pi}{4} d \frac{dE}{dx} \rho$  being the total energy deposition in the wire, the correction factor  $\frac{\pi}{4}$  comes from the fact that the distances on which energy is deposited are not always  $d$  as the cross-section of the wire is a circle, see yellow lines on Figure 4.1). This expression can be simplified, indeed, if the piece of the wire taken into account has a length of  $\Delta l$  (as in Figure 4.1)  $S_{CS} \cdot d = d^2 \cdot \Delta l$  and the volume  $V = \pi \cdot (\frac{d}{2})^2 \cdot \Delta l = \frac{\pi}{4} \cdot d^2 \cdot \Delta l$ . Finally,  $\left(\frac{\partial T}{\partial t}\right)_{\text{BH}}$  can be written like:

$$\left(\frac{\partial T}{\partial t}\right)_{\text{BH}} = \frac{\Phi(x, y, t)}{C_p(T)} \cdot \frac{dE}{dx}. \quad (4.4)$$

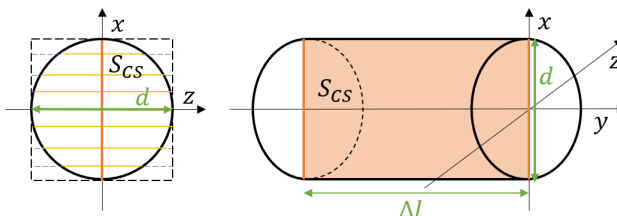


Figure 4.1: Diagram showing the cross-sectional area  $S_{CS}$  (in orange) of a piece of wire of length  $\Delta l$ . Yellow lines show some distances travelled by protons for the energy deposition. The diameter of the wire is  $d$ .

**Radiative cooling:** Caused by thermal radiation, this is a dominant cooling process up to temperatures of about 2000 K. It depends on the radiative surface  $S$ , the Stephan-Boltzmann constant  $\sigma_{SB} = 5.67 \cdot 10^{-8} \text{ W m}^{-2} \text{ K}^{-4}$ , the actual temperature of the wire  $T$ , the temperature of the surroundings  $T_0$ , the emissivity  $\epsilon(T)$ , the heat capacity  $C_p(T)$ , the material density  $\rho$  and the volume  $V$ .

$$\left( \frac{\partial T}{\partial t} \right)_{RC} = \frac{S \cdot \sigma_{SB} \cdot \epsilon(T) \cdot (T(x, y, t)^4 - T_0^4)}{\rho \cdot C_p(T) \cdot V}. \quad (4.5)$$

**Conductive cooling:** Caused by a spatial temperature gradient, it depends on the thermal conductivity of the material  $k(T)$  [ $\text{W m}^{-1} \text{ K}^{-1}$ ], the material density  $\rho$ , the heat capacity  $C_p(T)$  and the spatial temperature gradient in the wire direction  $\frac{\partial^2 T}{\partial y^2}$  [ $\text{K m}^{-2}$ ]:

$$\left( \frac{\partial T}{\partial t} \right)_{CC} = \frac{k(T)}{\rho \cdot C_p(T)} \cdot \frac{\partial^2 T}{\partial y^2}. \quad (4.6)$$

This process is neglected in this work due to the small cross-section of the thin wire.

**Thermionic cooling:** Due to electrons that are emitted from the wire when their thermal energy is sufficient to exceed the work function  $\phi(T)$  [eV] of the material, this emission will contribute to the cooling due to the energy taken by the escaping electrons. It depends on the radiative surface  $S$ , the work function  $\phi$ , the Boltzmann constant  $k_B = 1.38 \cdot 10^{-23} \text{ J K}^{-1}$ , the temperature of the wire  $T$ , the elementary charge  $Q_e$  [C], the thermionic current density  $J_{Th}(T)$  [ $\text{A cm}^{-2}$ ], which will be discussed more in details in Section 4.3, the density  $\rho$ , the volume  $V$  and the heat capacity  $C_p(T)$ .

$$\left( \frac{\partial T}{\partial t} \right)_{TC} = S \cdot (\phi + \frac{2k_B T}{Q_e}) \cdot \frac{J_{Th}(T)}{\rho \cdot C_p(T) \cdot V}. \quad (4.7)$$

This cooling process becomes dominant for high temperatures.

**Radio Frequency (RF) heating** The RF waves contained in the cyclotron resonators can leak to the rest of the machine, couple with the wire and heat it<sup>1</sup>. This RF heating in the case of RRL is so strong, that it makes the wire glow. This glowing is even apparent in visible light as shown in Figure 4.2. The vertical wire is the one that glows the most. Depending on the position of the scanner in the accelerator, this heating leads to wire temperatures in the range 530 - 1130 K [5]. This coupling phenomenon between the RF and the wire is a major problem that leads to recurrent wire breakage. It will not be discussed here because modelling requires specialised tools (e.g. CST studio) and has large uncertainties.

---

<sup>1</sup>In synchrotrons, such as the SPS or the LHC at CERN, RF heating is also observed, but the RF waves do not come from leaks in the resonators but from the beam wakefield.

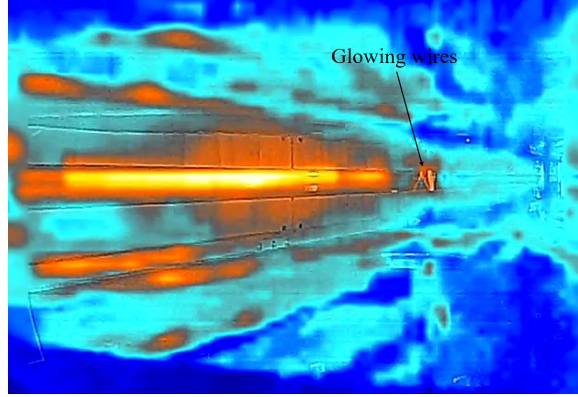


Figure 4.2: Image, taken using infrared camera FLIR AX8, of the glowing wires due to RF heating. No beam was present in the machine.

### 4.3 Wire signal: Secondary Emission and Thermionic Emission currents

In the case of wire scanners like RRL, when the beam energy is relatively low, the profile is reconstructed thanks to the current generated in the wire by its interaction with the particle beam.

The charge generated comes from two different sources: the emission of secondary electrons and the emission of thermionic electrons. Direct charge deposition is zero because the proton range in graphite at 72 MeV is 24 mm (from PSTAR [22]), 700 times larger than the thickness of the target.

**Secondary emission electron:** When the primary proton beam passes through the wire, secondary electrons may be emitted. Indeed, the energy transferred by the proton beam to the electrons in the wire may be enough for them to escape [18]. The Secondary Emission Yield (SEY) is the average number of electrons emitted per incident particle and it is computed thanks to the Sternglass formula [23]:

$$\text{SEY} = 0.01 \cdot L_S \cdot \frac{dE}{dx} \cdot \rho \cdot \left( 1 + \frac{1}{1 + 5.4 \cdot 10^{-6} \cdot \frac{E}{M}} \right) \quad (4.8)$$

with  $L_S = \frac{1}{3.68 \cdot 10^{-17} \cdot N_v \cdot Z^{\frac{1}{3}}}$  [cm] the characteristic length ( $N_v$  the number of atoms per unit volume and  $Z$  the atomic number),  $\frac{dE}{dx}$  [MeV cm<sup>2</sup> g<sup>-1</sup>] the stopping power,  $\rho$  [g cm<sup>-3</sup>], the density of the wire's material,  $E$  [eV] the kinetic energy and  $M$  [eV] the mass of the projectile.

When a projectile hits a target, the charge induced by secondary electron emission is given by [18]:

$$Q_{SE} = N_p \cdot \text{SEY}_p + N_p(1 - \eta)\text{SEY}_p + N_p \cdot BS_p \cdot \text{SEY}_p + \\ N_e \cdot \text{SEY}_e + N_e(1 - \mu)\text{SEY}_e + N_e \cdot BS_e \cdot \text{SEY}_e \quad (4.9)$$

$N_p$  is the number of protons of the projectile,  $N_e$  the number of electrons,  $\text{SEY}_p$

is the secondary emission yield of the proton, and  $\text{SEY}_e$  the one from electron,  $\eta$  is the portion of protons that stop in the material and  $\mu$  is the same for electron,  $BS_p$ , and  $BS_e$  are respectively the probability of back-scattered protons and electrons. In the case of a proton beam with zero probability of proton back-scattering and zero probability that the proton stops in the wire, charge generated by secondary emission can be expressed as follows:

$$Q_{SE} = 2 \cdot \text{SEY}. \quad (4.10)$$

The charge  $Q_{SE}$  described in equation (4.10) is the charge generated by one proton, so the number of protons passing through the wire and the current is proportional to the number of protons. This property is used to determine the transverse beam profile of the beam with RRL.

**Thermionic electron emission:** The other source of current in the wire is the thermionic current. The thermionic electron emission comes from electrons that gain enough thermal energy to break the work function and escape.

The current density is described by the Richardson and Dushman formula [6]:

$$J_{th} = A_R \cdot T^2 \cdot \exp\left(-\frac{\phi}{k_B T}\right). \quad (4.11)$$

$A_R = \frac{4 \cdot \pi \cdot m \cdot k_B^2 \cdot Q_e}{h^3} = 120.173 \text{ A cm}^{-2} \text{ K}^{-2}$  is the Richardson constant ( $m$  the mass of an electron,  $Q_e$  the elementary charge and  $h$  the Planck constant),  $\phi$  [eV] is the work function of the material,  $T$  the temperature and  $k_B$  the Boltzmann constant. At low temperatures, this current is really low, but because of its temperature dependence (with  $T^2$  and  $\exp\left(-\frac{\phi}{k_B T}\right)$ ), it becomes high as the temperature increases (see Figure 4.3). This behaviour might be an issue for the wire signal measurements. Indeed, unlike secondary emission, thermionic emission is not proportional to the particle density. If the wire reaches temperatures high enough to generate a thermionic current, the thermionic peak will deform measurements of the wire signals. The thermionic current appears only in extreme conditions, however, HIPA beams are very bright and thermionic current is an issue.

For RRL, to get rid of this thermionic current in order to have exploitable results a positive bias voltage is applied to the wire. This bias voltage will decrease the thermionic current by preventing electrons from escaping, however, this also affects the signal. Chapter 5 of this thesis has for objective to understand the effects of this bias voltage on the wire signal.

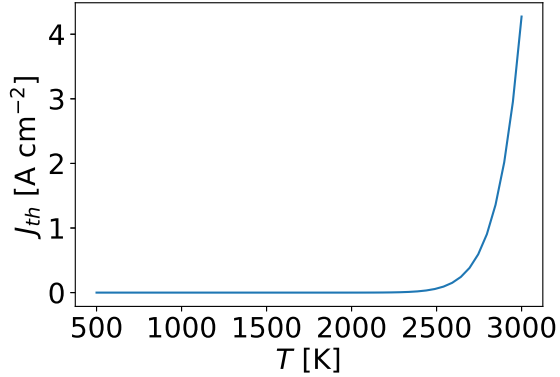


Figure 4.3: Thermionic current  $T_{th}$  in function of the temperature, computed with Richardson and Dushman formula (4.11) from [6].

For RRL, to get rid of this thermionic current in order to have exploitable results a positive bias voltage is applied to the wire. This bias voltage will decrease the thermionic current by preventing electrons from escaping, however, this also affects the signal. Chapter 5 of this thesis has for objective to understand the effects of this bias voltage on the wire signal.

### 4.3.1 The energy distribution of secondary and thermionic electrons

These electrons, which escape from the wire either by secondary emission or by thermionic emission, follow different energy distributions.

Secondary emission electron energy distribution is not well described by theory. Measurements show that it often depends on material and projectile properties [24]. The measurements for graphite and 100 MeV proton beam have not been found in the literature, therefore an approximate formula from [25] is used here:

$$f_{SE}(E) = \frac{E - E_F - \phi}{(E - E_F)^4} \quad (4.12)$$

with  $E$  [eV] the electron's kinetic energy,  $\phi$  [eV] the work function, and  $E_F$  [eV] the Fermi energy. If the reference point for the Fermi level is chosen just outside the material surface, the work function will be the opposite of the Fermi level [26].

For thermionic electrons, the energy distribution is proportional to [27]:

$$f_{Th}(E) = \frac{E - \phi}{1 + \exp\left(\frac{E - \phi}{k_B \cdot T}\right)} \cdot H(E - \phi) \quad (4.13)$$

which in this case depends on the temperature  $T$ .

In Figure 4.4 energy spectra of secondary and thermionic emission are represented. Secondary emission is normalised to 100 and for thermionic, values are normalised to 100 with respect to the one for 3000 K. The secondary emission spectrum has a peak around 1-2 eV, and it has a long high-energy tail. On the other hand, the energy corresponding to the peak for thermionic emission is lower than 1 eV and increases with higher temperatures.

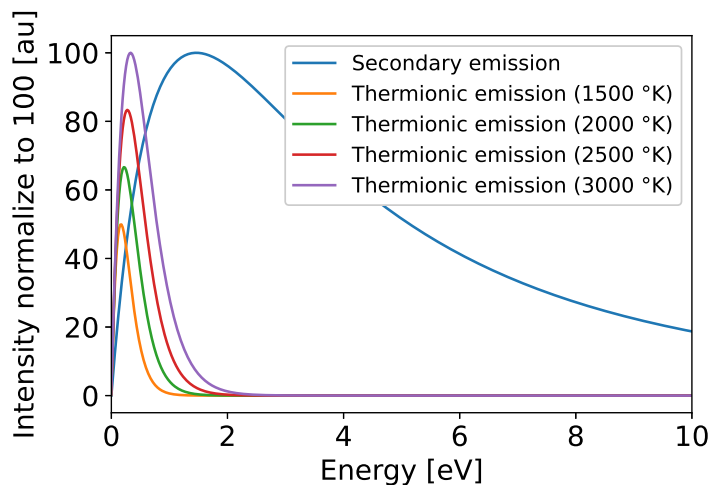


Figure 4.4: Energy spectra for secondary emission and thermionic emission electrons computed with Equations (4.12) and (4.13).

The above result (in Figure 4.4) suggests that a bias voltage of 2-3 V is enough to suppress thermionic emission, however, it would at the same time significantly

affect the secondary emission current, decreasing it by 25-40 %.

#### 4.4 Thermionic peak

In the case of wire scanners such as RRL, which use the current induced by the interaction between the beam and the target, it is important that the measured signal is proportional to the beam particle density. This condition is met when the only current generated in the wire is the secondary emission current, as described in Section 4.3. However, when the beam current increase, the temperature of the wire increases and thermionic electron emission can occur. Unlike secondary emission, this emission is not proportional to particle density. This emission leads to an additional contribution to the signal in the form of a thermionic peak illustrated in Figure 4.5.

The blue hatched area corresponds to thermionic electron emission. This peak distorts the Gaussian signal expected with only the secondary emission (orange hatched area in the same Figure).

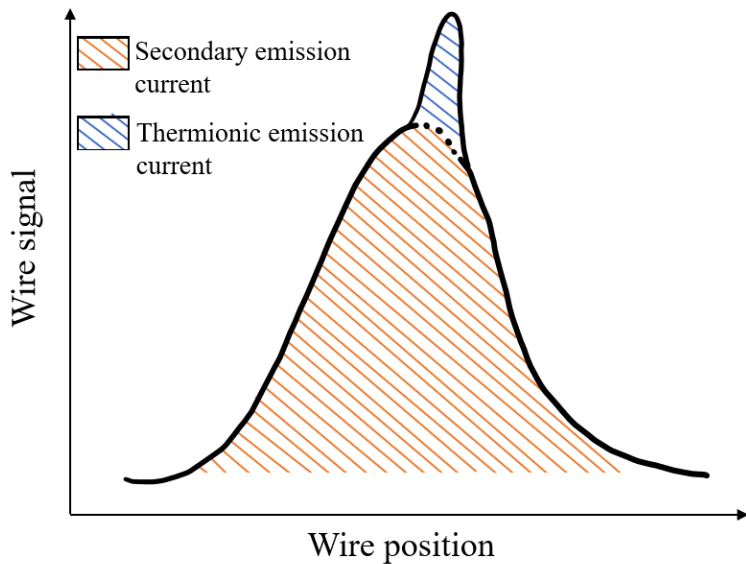


Figure 4.5: Illustration of the impact of strong thermionic emission on the measurement of transverse beam profile using wire scanner with wire current readout. In reality, both contributions cannot be distinguished, therefore thermionic emission leads to significant distortion of the measured beam profile.



# Chapter 5

## Observation of the influence of bias voltage on the wire signal

### 5.1 Application of the bias voltage

To get rid of the thermionic current, one solution is to apply a positive bias voltage to the wire. This bias counteracts the thermionic current by redirecting the low-energy escaping electrons back to the wire. This Chapter of the thesis will focus on the observation of wire signal at various bias voltages, this study and these results have been presented in an article for IPAC 2023 [28].

To show the effect of this bias voltage on the wire signal, RRL scans are studied. The data that are studied in this Chapter, and in all other Chapters that analyse data from RRL, have been taken in 2022 during the commissioning of RRL. Unfortunately, in 2023, the wires mounted in RRL break at each scan, due to the coupling between the wire and the RF. For this reason, there is no data from 2023 available.

After the scans, data are saved in a `xml` file and so that they can be analyzed using Python scripts created in Jupyter environment [29]. The signal from wire 1 is mainly used. Not all the scans taken in 2022 can be analysed, as some of them suffered a partial data loss after an interlock when the beam current is reduced to zero and there is no longer any detectable signal. And for some of them, wires were broken.

RRL can perform scans with several bias voltages. The bias is applied with a battery and 30 V, 60 V, and 90 V biases are studied. Those values are much higher than suggested in the previous Chapter (2-3 V). The reason is that the previous experience in which such biases were reducing the thermionic emission without affecting the signal. However, lower bias voltages will be investigated in the future.

At first sight, applying a bias voltage should cut the thermionic peak, but the secondary emission current should also be affected. Two orbits were selected to study the influence of the bias voltage on the wire signal. One with a small thermionic current in the absence of bias voltage, and the other with a large thermionic peak. These two orbits are orbit 10 (which corresponds to 105.6 MeV beam energy) and orbit 16 (which corresponds to 123 MeV). Energies are computed thanks to the equation (2.1). Orbit 16 has the largest thermionic peak of the scan. High-energy orbits often overlap, so they were not considered for analysis. These two peaks are

visible in Figure 5.1.

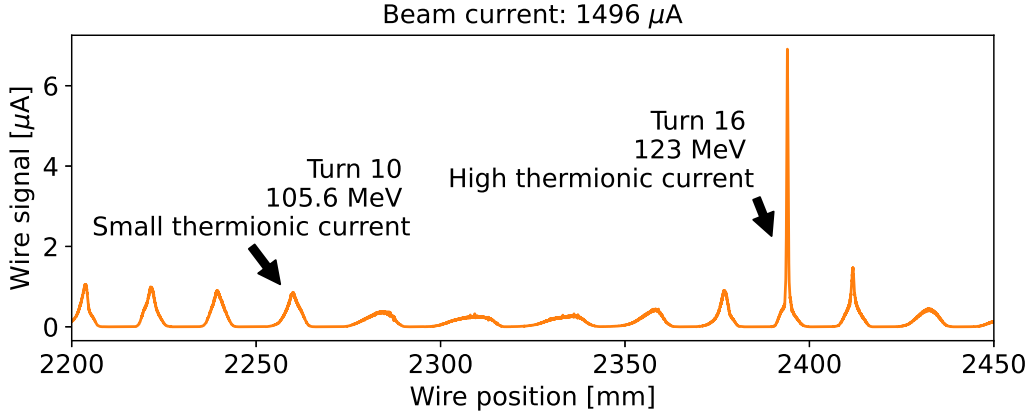


Figure 5.1: Extract of the scan of the profile with RRL, for  $1496 \mu\text{A}$  beam current and without bias voltage, orbits 10 and 16 are marked with an arrow.

The code called PyTT [7] which will be presented in detail in Chapter 6 is used to simulate the secondary emission current and the total current (secondary emission and thermionic emission). The code does not estimate the impact of the bias voltage.

Figure 5.2 shows orbit 10 for four scans with almost the same beam current and 4 values of bias voltages: no bias, with 30 V bias, with 60 V bias and with 90 V bias. The four peaks represent the signal for the same orbit, the positions are shifted to clearly distinguish the four scans on the same Figure and compare them more easily.

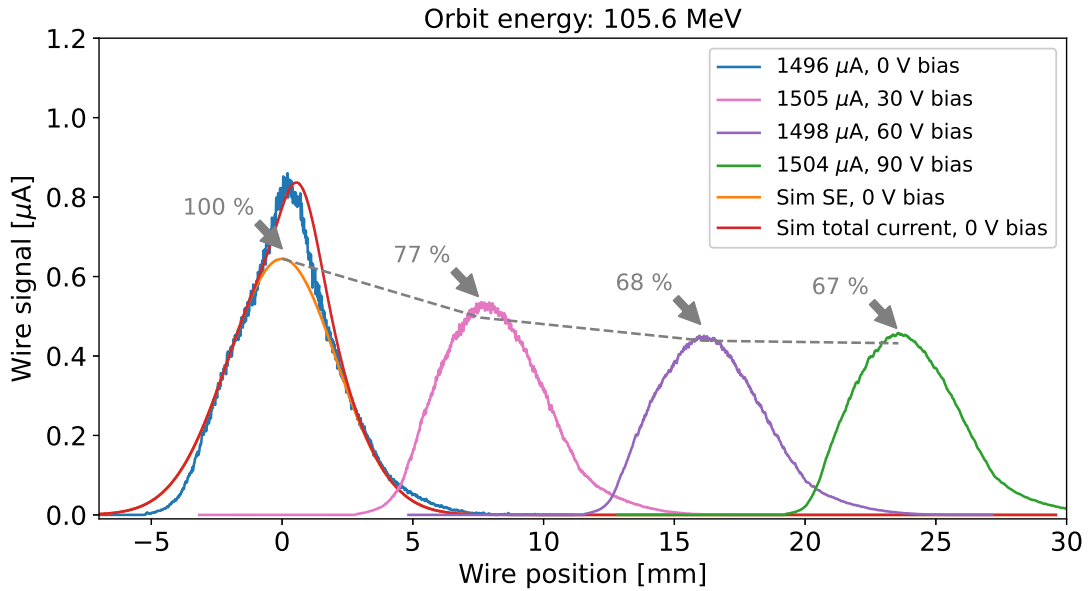


Figure 5.2: Wire signal for 4 different bias voltages, for orbit number 10 with  $\approx 1500 \mu\text{A}$  beam current, scan IN (wire moving from right to left).

The red curve represents the simulation of the total current (thermionic and secondary emission) for the case with no bias voltage, the orange curve represents

the simulated secondary emission current for the same case. The 30 V bias voltage seems to already suppress the thermionic current for this case, so applying a higher voltage here has no visible effect on the thermionic peak. Thanks to the simulation, it can be seen that the secondary emission is also affected by the bias voltage, with 30 V bias voltage it remains 77 % of the secondary emission current (compared to the simulated one). When bigger bias voltages are applied, secondary emission is still decreasing but it seems that it starts to stagnate and even higher voltages would not have a greater effect on the signal.

The case of a high thermionic peak is represented in Figure 5.3. As well as orbit 10, 4 scans with close currents ( $\approx 1500 \mu\text{A}$ ) and different bias voltages (0 V, 30 V, 60 V, and 90 V) of orbit 16 are shifted in position. As the thermionic current is much larger than the secondary emission current, a logarithmic scale is used for the wire signal axis, in order to correctly distinguish secondary emission and thermionic emission.

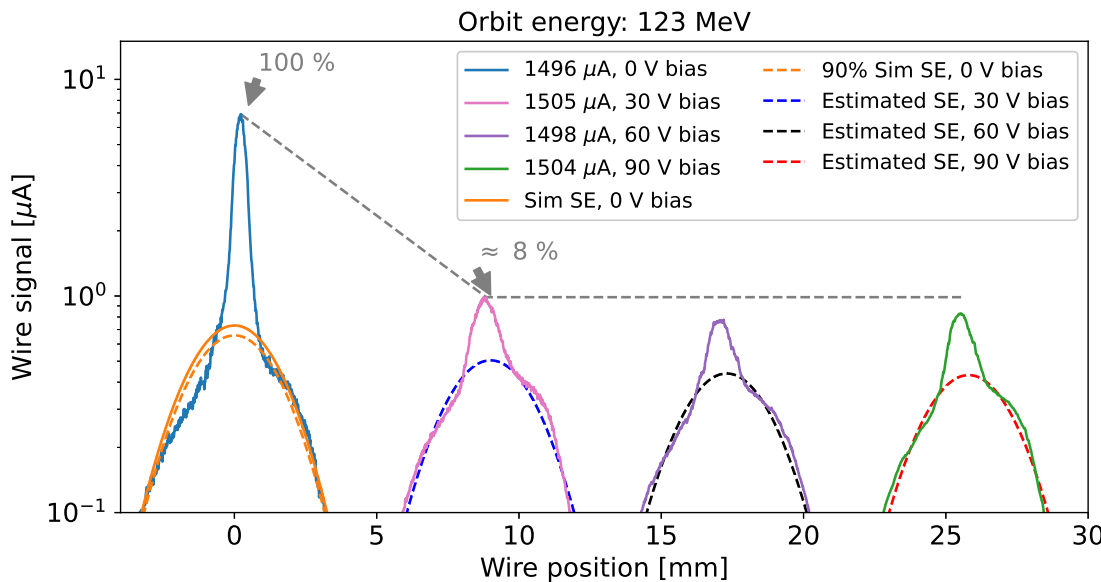


Figure 5.3: Wire signal for 4 different bias voltages, for orbit number 16 with  $\approx 1500 \mu\text{A}$  beam current, scan IN (wire moving from right to left).

The orange solid line represents the simulated secondary emission current. In Chapter 6, it will be discussed that for certain cases, the secondary emission current is overestimated by the simulation by PyTT, for that reason, the orange dotted line represents 90 % of the simulated secondary emission current. The estimated secondary emission currents (blue, black and red dotted lines) are computed by applying the percentages found in Figure 5.2 to the reduced simulated secondary electron current. These estimations should be treated with caution and should be regarded as an approximation since there is no proof that secondary emission current decreases with bias voltages in the same way for all orbits.

This Figure shows that for this high thermionic peak, bias voltage does not eliminate it completely, even with higher voltages. For each scan, there is a remaining bump and the increase of the bias voltage has no effect on it. This residual

thermionic current is estimated to be around 8 % of the initial thermionic current. This percentage is calculated by looking at the difference between the integral of the total signal and that of the estimated signal of the secondary emission.

## 5.2 Discussion

The reason for the remaining thermionic emission current may be the presence or absence of the bunch. This reasoning is inspired by R. Dölling and his article in the Proceedings of Cyclotrons2013 [30]. The bunch length in the Main Ring is about 200 mm ( $4\sigma_z$ ) which is about 8 % of the bunch spacing (20 ns). If the bunch does not overlap with the wire, applying a bias voltage will bring back the low-energy thermionic electrons to the wire. Indeed, thermionic electrons can be emitted even if there is no bunch passing through the wire because it depends only on the temperature of the wire, unlike secondary emissions electrons which require a bunch to pass through to be emitted.

If a bunch interacts with the wire thermionic and secondary emission currents will be generated and create the signal. A bunch of charged particles creates an additional transient electric field. This electric field and the potential associated, are computed thanks to the code Virtual-IPM from D. Vilsmeier [31] and are shown in Figure 5.4.

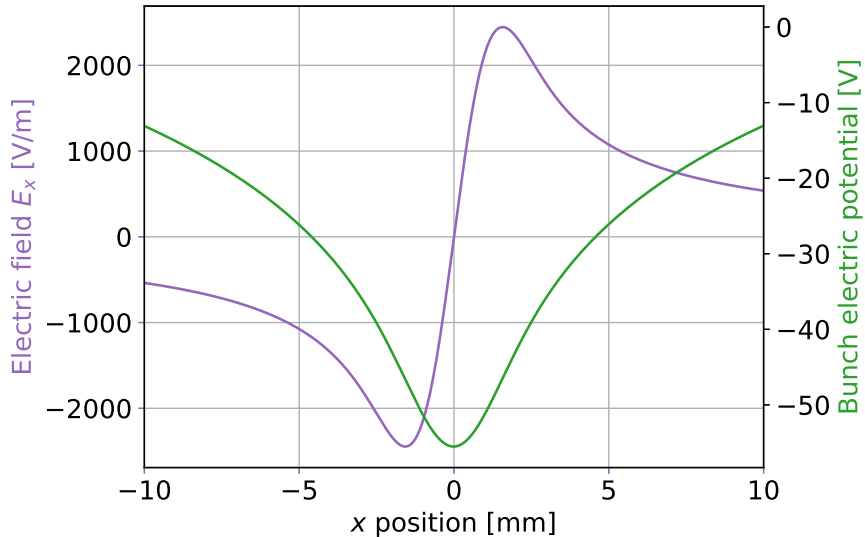


Figure 5.4: Bunch electric field and electric potential in the  $x$  direction, for 123 MeV beam energy and 1496  $\mu\text{A}$  beam current. The potential sign is inverted to express its "electron-trapping" capability.

Secondary electrons are generated promptly during the bunch passage and the bunch potential affects their trajectory to help them escape from the wire. For that reason, secondary electrons are strongly affected by the bunch potential.

As mentioned before, thermionic electrons can be emitted during the bunch passage and in-between bunches as this depends on the temperature of the wire. The bunch spacing is 20 ns, which is too short for the wire to cool down. So thermionic

emission occurs between bunches. As with secondary electrons, thermionic electrons can escape when there is a bunch, which is approximately 8% of the time, the rest of the time the bias voltage keeps them on the wire. In the case of orbit 16, the thermionic signal is reduced by more than 90 %, but if a higher voltage is applied, the remaining current does not disappear. It is also possible that a small part of the thermionic current remains in the case of orbit 10, but that it is too small to be distinguished.

Figure 5.5 shows the trajectories of the thermionic electrons computed with the Virtual IPM code when there is no beam passing through the wire. All the electrons travel only a few micrometres before being redirected to the wire. Tests to simulate the same thing with a beam passing through have been done but the results are not conclusive for the moment.

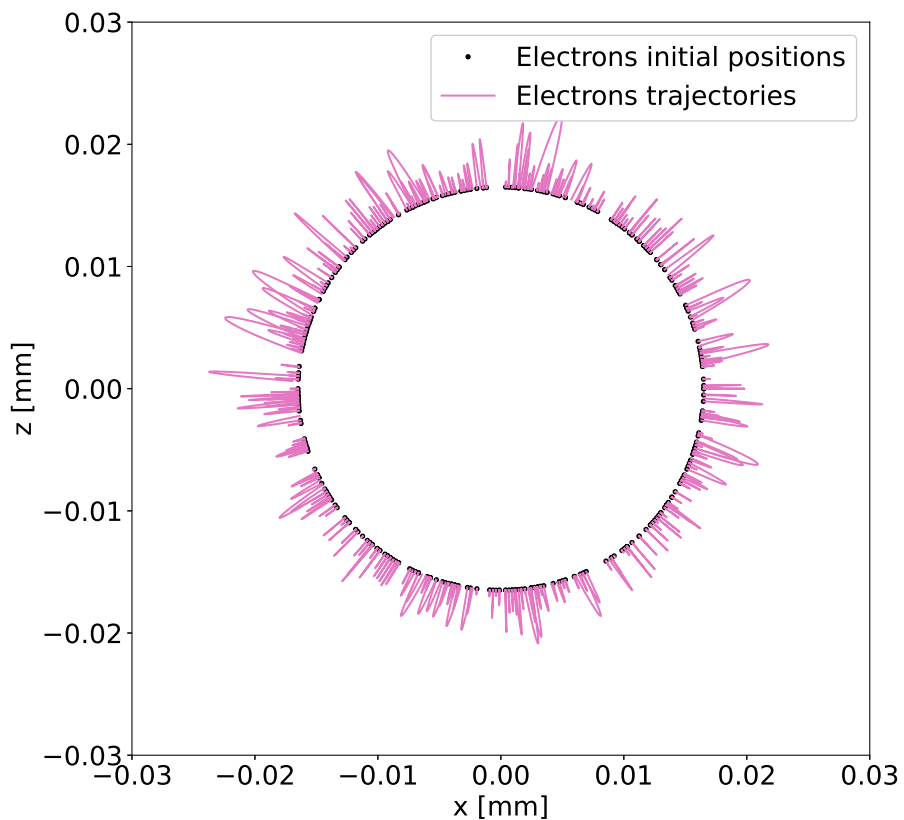


Figure 5.5: Escaping electrons trajectories from a 30 V biased wire simulated with Virtual IPM [31]. Electron initial velocity distribution is deduced by using the thermionic energy spectra (see Figure 4.4) for 1850 K wire temperature and initial positions are randomly set around a cylinder of diameter 34  $\mu\text{m}$ . Electrons are all coming back to the wire due to the electric field produced by the wire. No beam effects are taken into account.



# Chapter 6

## Simulations with PyTT

PyTT (which stands for Python Thin Target) is a Python Package implemented by M. Sapinski and A. Navarro and can be found on GitHub [7]. This numerical model simulates the thermal behaviour and the wire signal for thin targets used for beam instrumentation like wire scanners, SEM grid, and foils. With PyTT it is possible to simulate the temperature evolution of the thin target, and the signal (secondary and thermionic emission can be computed together or separately). The model is based on Finite Element Method. Thanks to the equations (4.2), (4.9) and (4.11), temperature and wire signals are computed in each "bin" composing the wire. For the case of the wire scanner simulations, there are no slices in the  $x$  direction transverse to the beam and in the  $z$  direction, the beam direction, because the wire is too thin (see Figure 6.2). So this is 1D code, but some preliminary extension to 2D has been added for the case of screens.

This code has been compared with the commercial software COMSOL in a master's project by A. Abouelenain [32] and the results of this benchmarking support its validity. In her PhD Thesis A. Navarro shows some experimental validation with a comparison of simulation and measurements for thermionic measurements at CERN LINAC4 [18]. Section 6.2 of this thesis presents also experimental validation of PyTT with RRL measurements.

This part of the report is dedicated to the simulations, the parameters required to simulate the thermal behaviour with PyTT, and the experimental benchmarking of this code.

### 6.1 Parameters

To carry out simulations with PyTT, several parameters are needed: firstly, the beam must be described, then the wire and the wire's material and a few other parameters like simulation steps must be determined.

#### 6.1.1 Beam parameters

**Bunch shape:** The beam type is the way in which the particles are distributed in the bunch. In most cases, bunches are in Gaussian shape and in particular, the transverse distribution of the particles follows a multivariate Gaussian distribution

in 2 dimensions centred at  $(x_0, y_0)$  which is described in equation (6.1):

$$P(x, y) = \frac{1}{2\pi \cdot \sigma_x \cdot \sigma_y} \exp\left(-\frac{(x - x_0)^2}{2 \cdot \sigma_x^2} - \frac{(y - y_0)^2}{2 \cdot \sigma_y^2}\right). \quad (6.1)$$

$\sigma_x$  and  $\sigma_y$  being the beam transverse sizes. One should remember that in cyclotrons the transverse beam shape can deviate from Gaussian. Here we assume beam to be Gaussian. The longitudinal beam shape plays no role in PyTT simulations.

**Beam transverse sizes:** The beam transverse sizes,  $\sigma_x$  and  $\sigma_y$ , are really important parameters. To set up a simulation, the sizes of the beam in the two transverse directions are needed. The measurements made with RRL give information about the size of the beam in the direction of the scan, horizontal ( $\sigma_x$ ) and also in the diagonal direction ( $\sigma_d$ , beam size in the diagonal direction) thanks to the two tilted wires.

The aim of this paragraph is to determine a formula from which  $\sigma_x$  and  $\sigma_d$  give  $\sigma_y$ , the vertical beam size. Isocontours of a multivariate Gaussian distribution in 2 dimensions are ellipses whose centre is  $(x_0, y_0)$  and whose axis are  $a = \sqrt{2}\sigma_x$  and  $b = \sqrt{2}\sigma_y$  [33] (see Figure 6.1). The diagonal axis ( $r(\theta = \frac{\pi}{4})$  in the Figure 6.1) is  $\sqrt{2}\sigma_d$ .

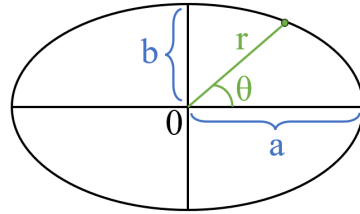


Figure 6.1: Ellipse.

The ellipse polar equation, if the reference frame is centred at 0, is:

$$r^2(\theta) = \frac{a^2 b^2}{a^2 \sin^2 \theta + b^2 \cos^2 \theta}. \quad (6.2)$$

If  $\theta = \frac{\pi}{4}$ , the diagonal axis is given by:

$$r^2(\theta = \frac{\pi}{4}) = \frac{a^2 b^2}{\frac{a^2}{2} + \frac{b^2}{2}} = \frac{2a^2 b^2}{a^2 + b^2}. \quad (6.3)$$

Then  $b$  can be isolated:

$$b = \sqrt{\frac{a^2 r^2}{2a^2 - r^2}}. \quad (6.4)$$

As  $r(\theta = \frac{\pi}{4}) = \sqrt{2}\sigma_d$ ,  $a = \sqrt{2}\sigma_x$  and  $b = \sqrt{2}\sigma_y$ , by replacing in equation (6.4), one gets:

$$\sigma_y = \sqrt{\frac{\sigma_x^2 \sigma_d^2}{2\sigma_x^2 - \sigma_d^2}}. \quad (6.5)$$

Computing the vertical beam size  $\sigma_y$  with the horizontal one  $\sigma_x$  and the diagonal one  $\sigma_d$  with equation (6.5) is to the detriment of a larger uncertainty for  $\sigma_y$  in the theoretical case of a horizontally narrow beam. If  $\sigma_x$  is very small, the diagonal size  $\sigma_d$  tends to  $\sqrt{2}\sigma_x$  and the uncertainty on  $\sigma_y$  would become very large. It is also possible to compute horizontal beam size  $\sigma_x$  if the measurements give  $\sigma_y$  and  $\sigma_d$  :

$$\sigma_x = \sqrt{\frac{\sigma_y^2 \sigma_d^2}{2\sigma_y^2 - \sigma_d^2}}. \quad (6.6)$$

**Beam size as a function of beam current:** When the beam current increases, the size of the beam increases too due to the space charge effect. However, at higher currents, there is thermionic emissions, and the beam profile, as measured by RRL, no longer follows a Gaussian shape, so it is not possible to determine  $\sigma_x$  and  $\sigma_y$ . Measurements of the beam size using various profile monitors were carried out with several currents at different locations along the beam lines [34]. These measurements show an empirical relation between beam size and beam current following a power law:

$$\sigma(I) = a \cdot I^b \quad (6.7)$$

with  $\sigma$  the beam size,  $I$  the beam current and  $a, b$  two constants. The exponent  $b$  seems to be really close to  $\frac{1}{3}$ . So, if the value of the beam size is measured for a smaller beam current ( $I_0$ ), and no thermionic emission is observed, it's possible to estimate the value of the constant  $a$  :

$$a = \frac{\sigma(I_0)}{I_0^{\frac{1}{3}}} \quad (6.8)$$

Then, equation (6.7) can be written like:

$$\sigma(I) = \sigma(I_0) \cdot \left( \frac{I}{I_0} \right)^{1/3} \quad (6.9)$$

By using the relation (6.9), the beam size can be found for bigger currents, when thermionic emission distorts the profile so much that direct measurement is impossible.

**The type of particle:** To describe the type of particle, the mass, the number of electrons and the number of protons that compose the particle is required. In the case of the PSI main ring cyclotron, particles are protons, with a mass of  $1.27 \cdot 10^{-27}$  kg.

**The beam energy:** The beam energy is needed to compute the correct stopping power  $\frac{dE}{dx}$ . Values of stopping power from NIST (PSTAR) [22] are used for beam energy from 0.001 MeV to 10000 MeV. For PSI's Main Ring Cyclotron, beam energy goes from 72 MeV to 590 MeV and can be computed for each orbit thanks to the equation (2.1).

**Number of particles in the beam or intensity:** The code needs either the number of particles in the beam circulating in a synchrotron or the beam current in the case of linacs or cyclotrons. If the beam current  $I$  is given, the equivalent number of particles  $N$  will be computed:

$$N = \frac{I \cdot t}{Q_e} \quad (6.10)$$

with  $t$  the total duration of simulation and  $Q_e = 1.602 \cdot 10^{-19}$  C the elementary charge.

### 6.1.2 Wire parameters

For the wire, the parameters are:

- The wire material
- The initial position of the wire
- The final position of the wire
- The wire length
- The wire diameter
- The wire resolution, the size of a slice/elements for the finite elements method simulations
- The wire speed

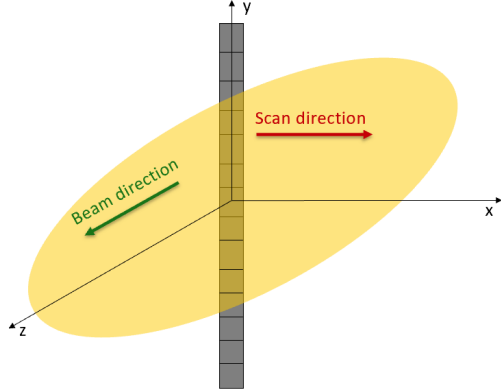


Figure 6.2: Drawing of the wire with slices and the beam.

### 6.1.3 Wire's material parameters

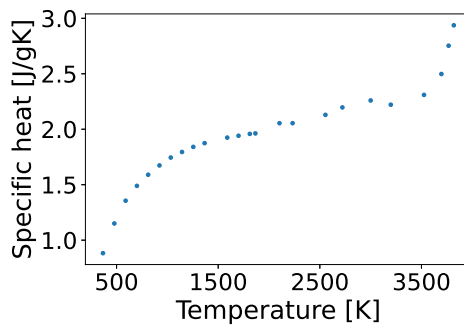


Figure 6.3: Specific heat as a function of the temperature [35].

Defining the material is an important step. The RRL's wire is made of carbon fibre. The atomic number of carbon is 6 and the molar mass is 12.0107 u. The density of this carbon fibre is  $2.1 \text{ g cm}^{-3}$ . Three other crucial parameters have to be taken into account: the specific heat  $C_p(T)$ , the emissivity  $\epsilon$ , and the work function  $\phi$ . The values for the specific heat as a function of the temperature are taken from TPRC Data Series [35] (Figure 6.3). For the emissivity, the value of 0.8 [36], [37] is used, this is a simplified assumption.

For the work function, things are much more complicated, indeed, the work function seems to decrease with temperature as the literature suggests [38], [39]. However, no exact behaviour for carbon fibres used in RRL is known. The evolution could be linear as a function of the temperature [38], or even quadratic [39]. Two behaviours are tested (see Figure 6.4):

- Linear  $\phi = \phi_0(1 - \beta T)$  with  $\phi_0 = 6$  eV the work function at  $T = 0$  K and  $\beta = 9 \cdot 10^{-5}$
- Quadratic  $\phi = \phi_0 - \gamma \frac{k_B T^2}{\phi_0}$  with  $\phi_0 = 6$  eV and  $\gamma = 180$ .

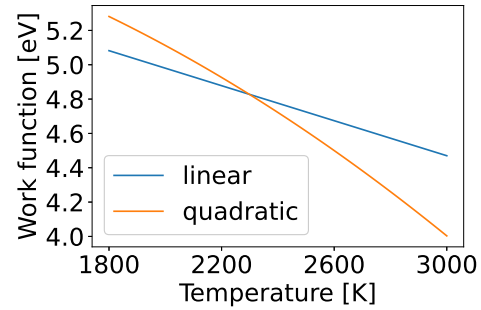


Figure 6.4: Work function temperature dependence for quadratic and linear behaviour.

#### 6.1.4 Other parameters

The initial wire temperature  $T_0$  is set to 1030 K, which is due to the RF heating (see Figure 6 from [5]). The user has to decide which cooling process is useful and needs to be included, in most cases only radiative and thermionic cooling are used, conductive cooling has a negligible effect due to the small wire cross-section. For the type of wire scanner such as RRL, the number of time steps is defined inside the code, for the following simulations it is set to 10000.

The Graphical User Interface of PyTT can be seen in Figure 6.5.

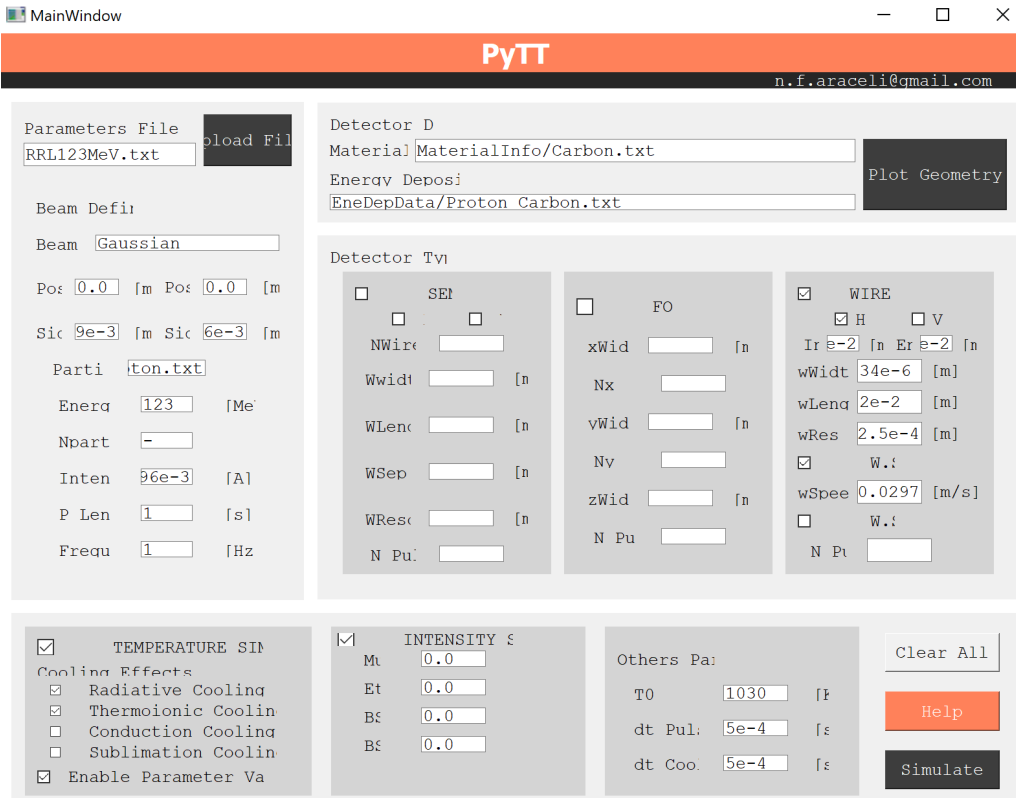


Figure 6.5: Graphical User Interface (GUI) of PyTT [7].

## 6.2 Benchmarking

In order to validate and test the code a benchmarking is done. The code can simulate the temperature and the wire signal. To carry out this benchmarking, measurements from RRL are compared with the simulations, but as it is difficult to measure the temperature evolution of the wire, the wire signal is used. We are looking if the registered signals, particularly the thermionic components, agree with the measurements. The agreement is an evidence that the temperature calculation is correct. The study is focused on wire 1, the vertical one.

### 6.2.1 Presentation of the three chosen cases

Simulation is done for particular orbits, not for the whole scan. Wire cools down between crossing consecutive orbits. Three cases are studied for this benchmarking:

- A case with **no thermionic current**, only secondary emission. The orbit chosen is orbit number 10 of a scan with  $413 \mu\text{A}$  beam current, which corresponds to 105.6 MeV beam energy. This peak is marked with an arrow in Figure 6.6 which represents an extract of the scan with  $413 \mu\text{A}$  beam current for the wire 1. As it is a relatively small current and there is no thermionic emission, it is possible to determine the horizontal and diagonal beam size ( $\sigma_x$  and  $\sigma_d$ ) by applying a Gaussian fit to the measurement of the wire signal of wires 1 and 2, without forgetting that the signal obtained from the diagonal wires must be divided by  $\sqrt{2}$ . With that, the vertical beam size  $\sigma_y$  is computed thanks to equation (6.5). The stopping power  $\frac{dE}{dx}$  for a 105.6 MeV proton beam in carbon fibre is  $6.231 \text{ MeV cm}^2 \text{ g}^{-1}$ .
- A case with **a small thermionic current**. This time, the beam current is  $1496 \mu\text{A}$ , and the orbit is again the number 10 (105.6 MeV beam energy). This peak is visible in Figure 6.7 (an extract of the  $1496 \mu\text{A}$  beam current scan for the wire 1), the one indicated by an arrow on the left. To obtain the size of the beam, equation (6.9) is used, by determining the  $a$  constant with the beam size of orbit 10 wire signal with  $413 \mu\text{A}$  beam current. The stopping power is  $6.231 \text{ MeV cm}^2 \text{ g}^{-1}$ , as for the case before because this is the same beam energy.
- The last case is with **a big thermionic current**. It corresponds to orbit number 16 (123 MeV beam energy) with  $1496 \mu\text{A}$  beam current. This peak is indicated in Figure 6.7 with an arrow on the right. Orbit number 16 is, for the majority of the scans, the orbit with the highest thermionic peak. The beam sizes are found with equation (6.9), by using the beam sizes of the wire signal of orbit 16 for the scan at  $413 \mu\text{A}$  beam current. The stopping power of a 123 MeV proton beam in carbon fibre is  $5.575 \text{ MeV cm}^2 \text{ g}^{-1}$ .

The last two cases are the same studied in Chapter 5 on the influence of the bias voltage on the wire signal.

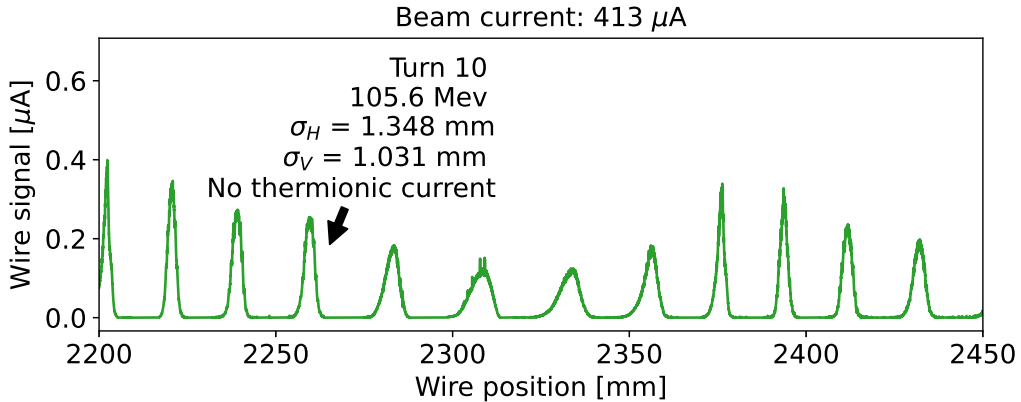


Figure 6.6: Extract from RRL’s wire 1 scan with  $413 \mu\text{A}$  beam current.

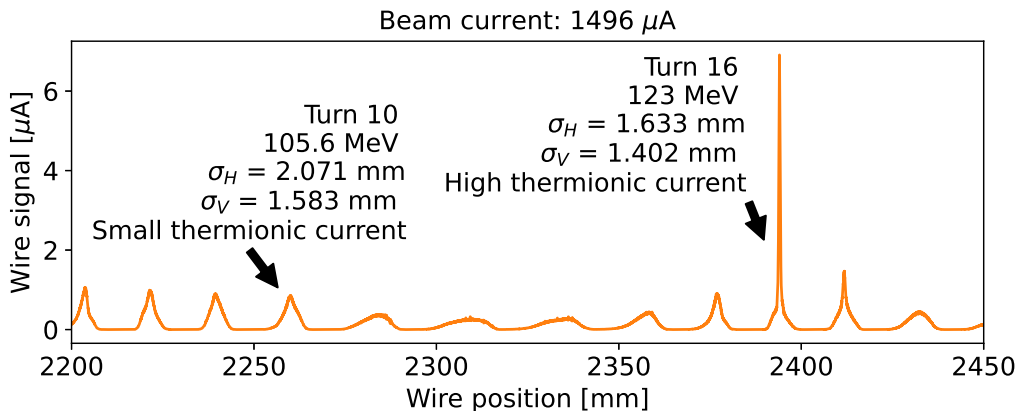


Figure 6.7: Extract from RRL’s wire 1 scan with  $1496 \mu\text{A}$  beam current.

### 6.2.2 Results of the simulations

Simulations with PyTT are done with the same beam parameters to compare simulation results with measurements. The following Figures were presented in the article for IPAC 2023 [28]. As a reminder, the target is  $34 \mu\text{m}$  diameter wire made of carbon fibre with a speed of  $2.97 \text{ cm s}^{-1}$ . One simulation is done for each case, and the central position is the centre of the beam. Post-processing is done to match the position of the wire in simulation and in measurements. For simulation, a 2 cm long wire is sufficient to cover the entire beam, obviously in reality the wire is longer (8.8 cm) in order to be mounted correctly on the trolleys. The wire binning is 0.25 mm. The number of time steps is set to 10000. The results of the simulation compared to measurements for the three cases can be seen in Figures 6.8, 6.9, and 6.10.

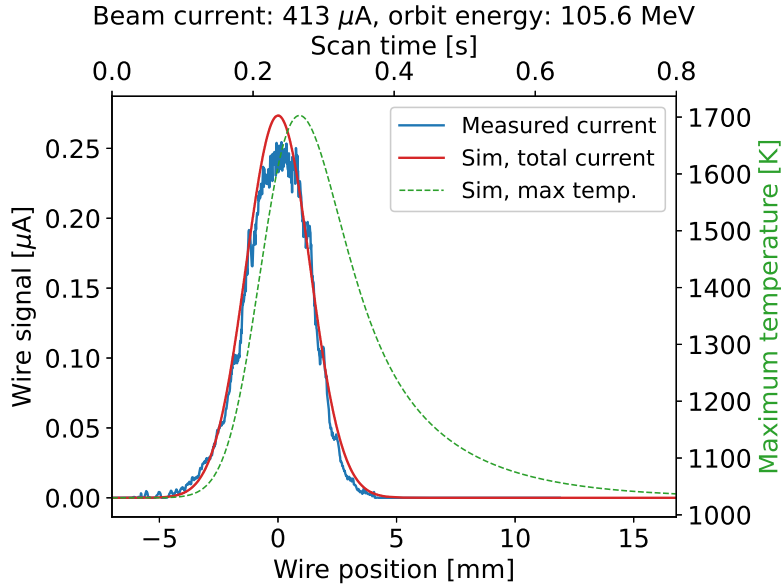


Figure 6.8: Simulation and measurement of the wire signal for  $413 \mu\text{A}$  beam current for orbit 10. No thermionic current is observed.

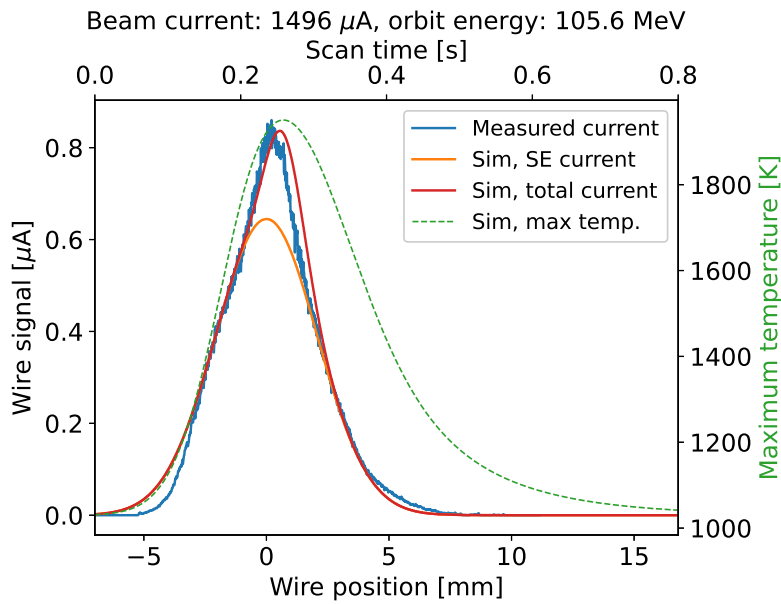


Figure 6.9: Simulation and measurement of the wire signal for  $1496 \mu\text{A}$  beam current for orbit 10. A small thermionic current is observed. Only a quadratic temperature dependence work function is used.

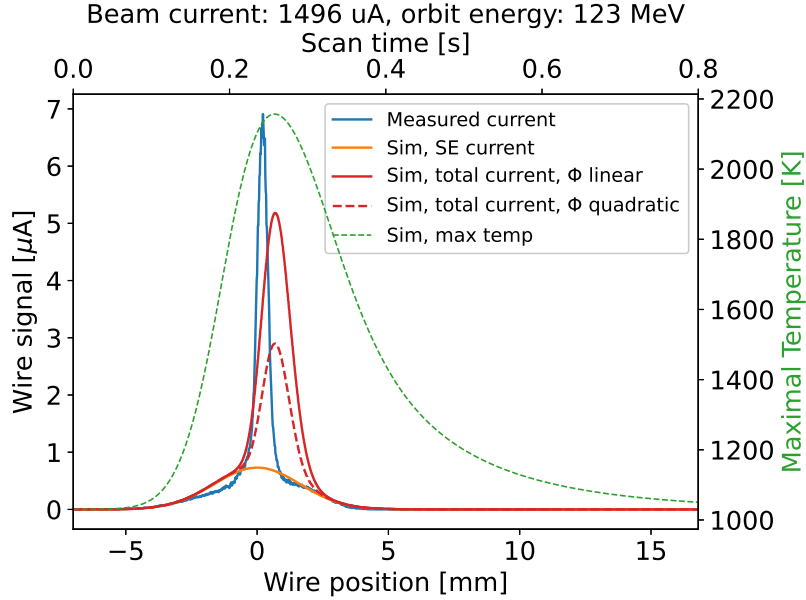


Figure 6.10: Simulation and measurement of the wire signal for  $1496 \mu\text{A}$  beam current for orbit 16. Large thermionic current does not allow for beam profile determination.

### 6.2.3 Comparison with measurements and discussion

For the case with no thermionic current (Figure 6.8), the shape of the wire signal is well reproduced. As for measurements, the code gives no thermionic peak for this orbit at this beam current. However, the simulated current (red curve) is slightly higher than the measured one. This can be due to a ohmic loss of the measured current over the carbon fiber ( $\approx 2 \text{k}\Omega$ ) or over 86 m cable between the wire and the current meter. The simulated maximum temperature of the wire is also plotted and the wire reaches a temperature around 1700 K at maximum.

Figure 6.9 shows the wire signal when there is a small thermionic peak. Two simulated currents are plotted, one for the total current (secondary emission current and thermionic current), the red curve, and the other one which represents only the secondary emission current, the orange curve. These results show that small thermionic peaks are accurately reproduced by PyTT. The maximum temperature reached by the wire is close to 2000 K.

In Figure 6.10 the biggest thermionic peak is visible. This peak is narrow but has a very high intensity compared to the secondary emission current. As is visible in this Figure, the simulation code does not reproduce accurately the thermionic peak. The simulated secondary emission current (orange curve) seems to be slightly higher than the measured one, like for the first case with only secondary emission. When all currents are taken into account, the simulated thermionic peak is wider than the measured one and amplitudes are not the same for both work function temperature dependence. This discrepancy could come from two main problems:

- As written before, the work function of carbon fibre is not well known, especially the temperature dependency, and as it is shown the thermionic current

has a high sensitivity on this parameter. It could also come from emissivity temperature dependence which is not taken into account and as for work function, the temperature evolution is not known. This high sensitivity is discussed in the next Section.

- Another source of error might come from phenomena that are not simulated by PyTT. Indeed, the emitted electrons can create a cloud around the wire. This phenomenon, called a space charge, creates a potential barrier for other electrons to be emitted. This, and other phenomena, may temporarily increase the electron reflection coefficient, resulting in a decrease of the thermionic peak amplitude and width.

#### 6.2.4 Wire signal's high sensitivity on work function and emissivity

The goal of this Section is to see how changes in the work function and emissivity can affect the maximal temperature of the wire and the maximum of the wire current. Figure 6.11 plots the relative error induced on the simulated maximum temperature and on the simulated maximum wire current, as a function of the relative error on the work function. The initial value of the work function chosen (i.e. when there is no relative error) is 5 eV. For this study, a constant value of the work function is chosen to simplify the study as the evolution as a function of temperature is not well determined.

Figure 6.12 shows the same thing, but this time as a function of the relative error in emissivity. The initial value is 0.8.

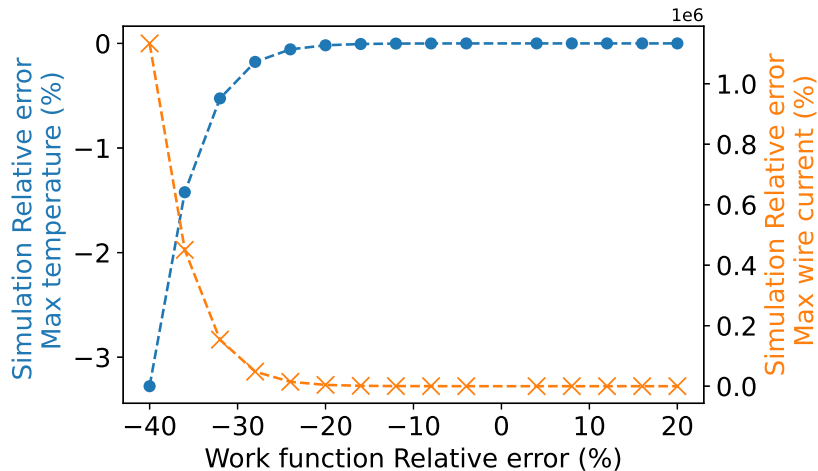


Figure 6.11: Simulated maximum temperature relative error and simulated maximum wire current relative error in function of the work function relative error, the initial work function (= 0 % relative error) is the constant 5 eV.

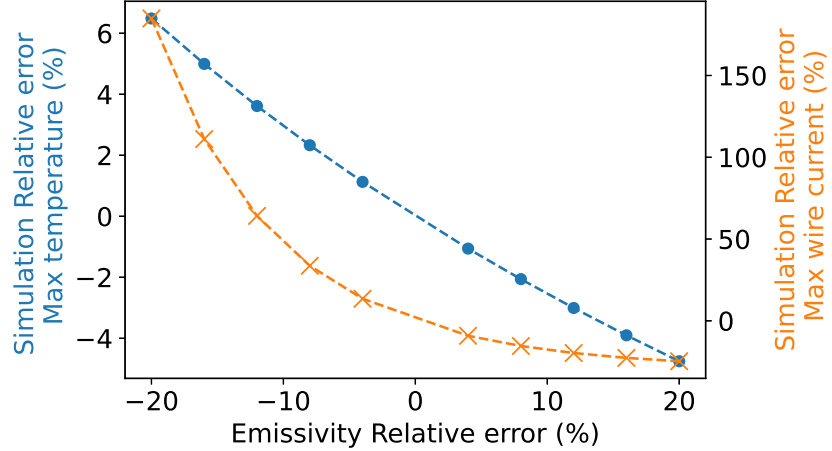


Figure 6.12: Simulated maximum temperature relative error and simulated maximum wire current relative error in function of the emissivity relative error, the initial emissivity (= 0 % relative error) is 0.8.

In both cases, work function and emissivity, the effect on the temperature is smaller than the effect on the wire current.

For the work function case, when the value of the work function decreases (negative relative error), the evolution of the relative error of the temperature and of the wire signal follows an exponential behaviour, this is due to the exponential dependence of the thermionic current. However, the values for the temperature and the wire signal are not at all the same: for the temperature, the error does not exceed 3 %, whereas for the wire current, i.e. the current generated, the relative error exceeds  $10^6$  % when the work function decreases by 40 %.

When the value of the work function increase (positive relative error), as there is no more thermionic emission, relative errors become really small, because the work function has no influence on the secondary emission current.

In terms of emissivity, the relative error is larger when emissivity decreases than when it increases. The evolution is linear for the temperature relative error.

This study of relative errors highlights the great sensitivity of the simulations to variations in certain parameters such as the work function and emissivity. As long as these parameters are not described precisely and the behaviour as a function of temperature is not properly detailed, the simulation results should be treated with caution.

### 6.3 Wire diameter study

As written in Chapter 5, the thermionic current is not completely suppressed by the bias voltage. One solution to avoid thermionic emission could be to reduce the diameter of the wire, in this way, the temperature reached by the wire will be lower and then the thermionic current will also decrease.

PyTT simulations are done with various wire diameters to estimate what should be the ideal thickness of the wire. The used case is the one with the highest thermionic peak (orbit 16, with 123 beam energy and 1496  $\mu\text{A}$  beam current). For simplification, it is assumed that the work function is a constant, and the value 4.78 eV is chosen to match the amplitude of the measurements done with RRL (see blue curve in Figure 6.10) with a 34  $\mu\text{m}$  diameter wire. Wire diameter varies between 34  $\mu\text{m}$  and 12  $\mu\text{m}$ .

In Figure 6.13 the simulated wire current is plotted for various wire diameters. In Figure 6.14 total current and only secondary electron emission are plotted for the smallest diameters. One can observe that the thermionic emission becomes very low or non-existent with 14, 13 or 12  $\mu\text{m}$  diameter wires.

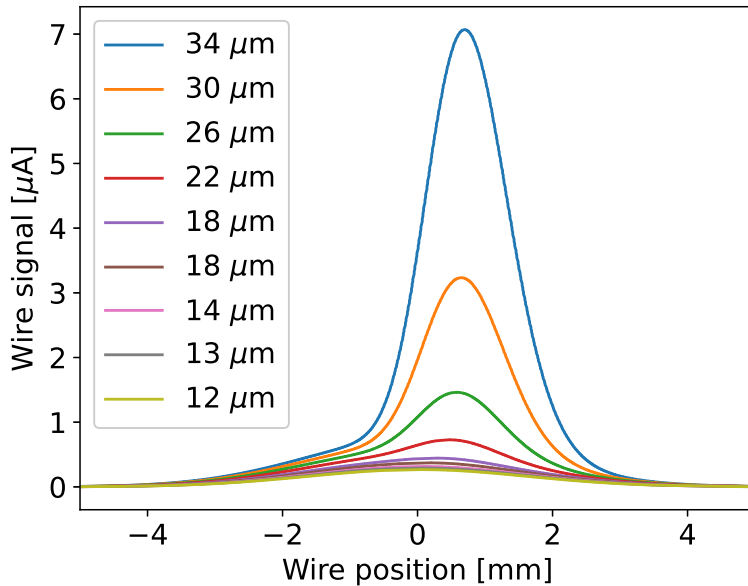


Figure 6.13: Wire signal for various wire diameters between 34  $\mu\text{m}$  and 12  $\mu\text{m}$  for a beam with 123 MeV energy and 1496  $\mu\text{A}$  current.

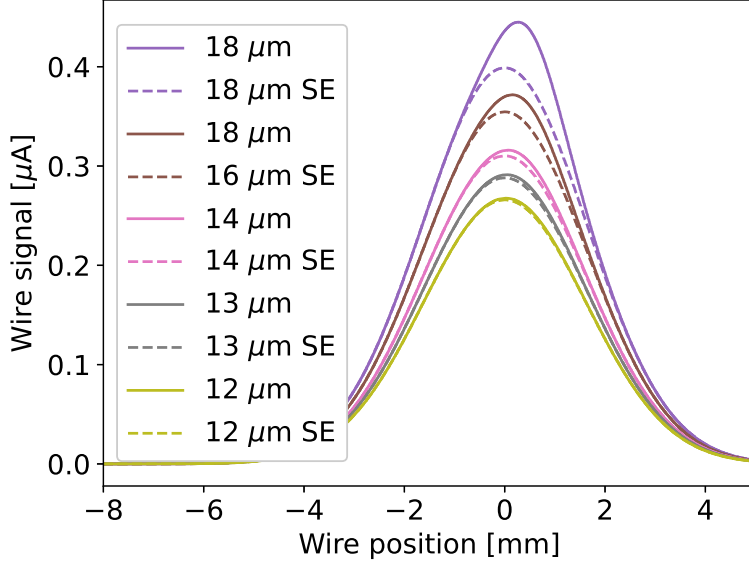


Figure 6.14: Wire signal for various wire diameters between  $18 \mu\text{m}$  and  $12 \mu\text{m}$  for a beam with 123 MeV energy and  $1496 \mu\text{A}$  current. Solid lines show the total wire current and dotted lines show only secondary emission current.

The typical operational beam current is 1.8-2.0 mA, but even 2.4 mA has been already reached. In Figure 6.15 diameters between 34 and 8  $\mu\text{m}$  are tested for this extreme current. Only wire signals with the smallest diameters are shown in Figure 6.16. With an 8  $\mu\text{m}$  wire, there is no more thermionic emission.

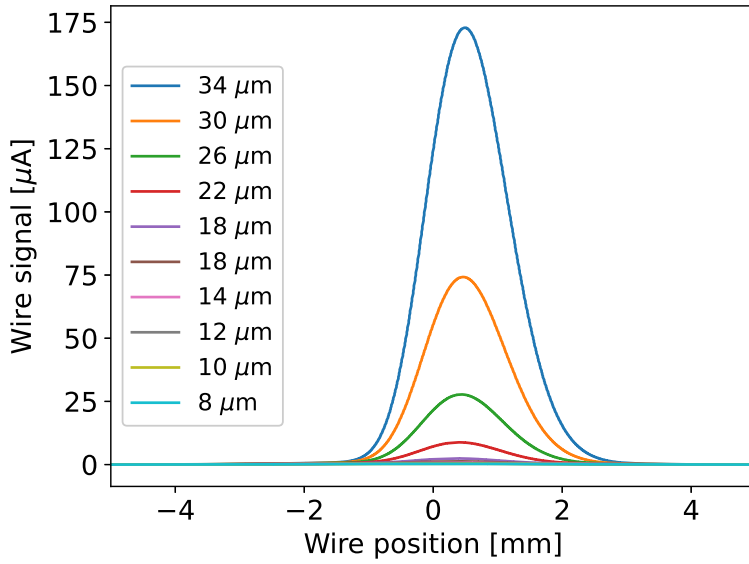


Figure 6.15: Wire signal for various wire diameters between  $34 \mu\text{m}$  and  $8 \mu\text{m}$  for a beam with 123 MeV energy and 2.4 mA current.

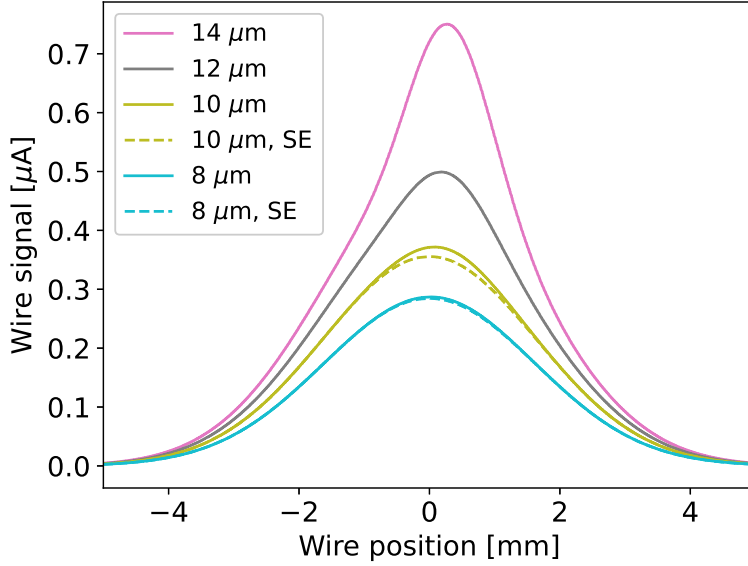


Figure 6.16: Wire signal for various wire diameters between  $14 \mu\text{m}$  and  $8 \mu\text{m}$  for a beam with 123 MeV energy and 2.4 mA current. Solid lines show the total wire current and dotted lines show only secondary emission current.

Reducing the diameter of the wire could be a solution against thermionic emission, however, really thin wires are very difficult to be mounted on the trolleys and wires have less mechanical strength making them weaker. Moreover, if the beam current in the machine increases in the future the diameter of the wire must be thinner and thinner to avoid thermionic emission.

To avoid the problems that a wire with a smaller diameter could bring, another solution to suppress thermal emissions could be to change the material of the wire. This is studied in the next Chapter.

# Chapter 7

## Low-density materials as wire scanners target

Wire scanner targets are typically made of carbon fibre, molybdenum or tungsten. These materials are chosen for their electrical, mechanical and thermal properties. However, these materials can reach their limits, break or in other ways not satisfy the conditions required for the probe to work properly. For example, carbon fibre wires can suffer from sublimation, as is shown in [40] and molybdenum wires can have ductile breakage at high temperatures like in [41]. Even if wires don't break signals can be disturbed by thermionic electron emission.

To overcome the problems encountered with 'traditional' materials, one solution is to change the material that constitutes the wire. Low-density materials are good candidates for solving these problems. In particular, carbon nanotube appear to be a particularly interesting choice. This material, which depending on the manufacturing method, has a lower density than carbon fibre and potentially is stronger, could be used to make wires that could be used in wire scanners. This Chapter is devoted to comparing the thermal behaviour of carbon fibres with carbon nanotube as wire scanner targets.

Thanks to the PyTT program, simulations are being carried out for different beams to study how low-density materials can improve the measurements made by wire scanners in certain cases. These results were presented at the Low-density Materials for Beam Instrumentation workshop at CERN on 20 and 21 June 2023 [42].

### 7.1 Materials parameters

For the following simulations, two types of material are used as wire scanner targets: carbon fibres (CF) and carbon nanotube (CNT) wires. As mentioned in Chapter 6, for PyTT, the material is defined by its density, its specific heat, its work function and its emissivity. All these properties are examined in the paragraphs below.

**Density:** For carbon fibre wires, a density of  $2.1 \text{ g cm}^{-3}$  is used, as in previous experiments. For carbon nanotube wires, 2 cases are taken into account:

- A case with a density of  $1 \text{ g cm}^{-3}$  which corresponds to the density of carbon nanotube wires used in experiments at CERN carried out by A. Mariet for

his PhD thesis [43]. In this case, the samples were contaminated with iron, a material that served as a substrate for the growth of the CNT. This contamination increases the density and also he made the hypothesis that it could lead to faster damage of the wire when it is exposed to a beam.

- For the other case, a density of  $0.2 \text{ g cm}^{-3}$  is used, this corresponds to an anticipated case, of nanotube wires that could exist later on the market [44]. These ultra-long CNTs (14 cm) that could compose this wire were investigated using SEM at PSI with the help of E. Müller and Electron Microscopy and Diffraction group (see Figure 7.1). In this Figure, one can see carbon nanotubes linked together to form bigger strands, and other parts where there is no order. To be used as wire scanners targets one has to find a way to bind them to form a wire.

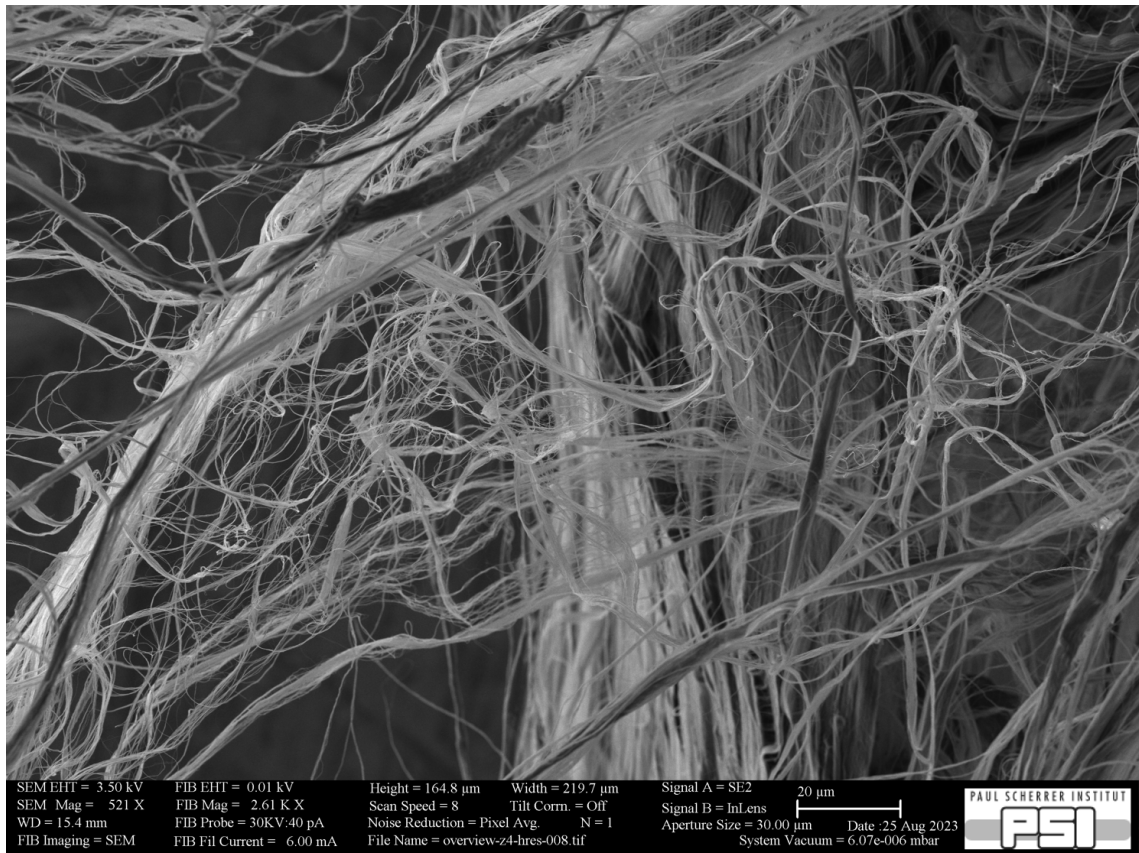


Figure 7.1: SEM image of CNT from [44], with a magnification of 521.

**Specific heat:** Due to the lack of data the specific heat is assumed to be the same for both materials. The values are taken from the TPRC data series [35] (see Figure 6.3).

**The emissivity:** It is the same for both materials and for these simulations, the value used is 1 as in the first approximation the wires are black. However, emissivity

is a parameter that will depend on the surface of the wire. If the wire has irregularities, the emissivity can drop. Carbon nanotube wires can have many surface irregularities (see Figure 7.2, a SEM picture of the surface of a CNT wire, where irregularities are visible) and the emissivity could be lower.

**Work function:** The work function is defined as constant and the same for both materials (5 eV). However, as with emissivity, irregularities on the surface of the wire can cause the value of the work function to decrease. Therefore, potentially CNT wires can have a lower work function than CF. In addition, as discussed in Benchmarking, Chapter 6, according to various sources in the literature [39], [45], the work function is supposed to decrease as the temperature of the material increases. However, this behaviour is not precisely known for CF and no data at all were found for CNT, so for the sake of comparison the same constant value is taken for both materials.

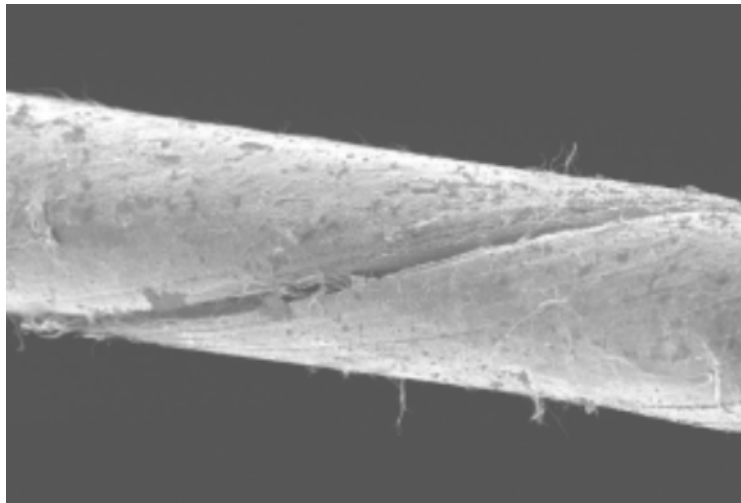


Figure 7.2: SEM picture of the surface state of 30  $\mu\text{m}$  diameter CNT wires, irregularities at the wire surface are visible. (Courtesy of Alexandre Mariet, from [43]).

With these assumptions, the materials are compared based only on the density difference.

## 7.2 Beam parameters

To compare the thermal behaviour of CF and CNT, several beams were simulated.

Firstly, beams from PSI's Main Ring Cyclotron, orbit 10 (105.6 MeV energy beam) and 16 (123 MeV beam energy) were used with a current of 1496  $\mu\text{A}$ . Those are the same beam conditions as used to investigate bias voltage in Chapter 5 and for the PyTT code benchmarking in Chapter 6. To go further, a beam with a current of 5 mA is simulated, corresponding to a current that could be reached by a future cyclotron used for accelerator-driven systems (ADS) [46]. The aim of ADS is to produce nuclear energy using thorium and producing very little radioactive waste. A proton beam produced by a cyclotron will lead to the production of a neutron beam by spallation, and these neutrons will carry out the transmutation. For the

sake of comparison and due to the lack of data on the beam in ADS, a 123 MeV beam is also taken into account here. Sizes of the beam are extrapolated from PSI's main ring using equation (6.9), and the beam sizes of orbit 16 at 413  $\mu\text{A}$  beam current.

The future HL-LHC (High Luminosity Large Hadron Collider) beam is then simulated. The HL-LHC is the project for the next upgrade of the LHC [47], which involves increasing the nominal luminosity of the LHC by a factor of 5 to 7.5. To achieve this goal, the nominal beam intensity will be multiplied by 2. The instrumentation put in place for the LHC cannot be adapted for the HL-LHC, so it is essential to find new ways of measuring the beam parameters. The use of new materials, such as low-density materials, could also be a possible solution for this project. The beam used corresponds to the beam at injection, i.e. with an energy of 450 GeV, and as far as the intensity is concerned, only 25 % of the nominal current is taken into account.

All information on simulated beam parameters is listed in the "Beam parameters" section of Table 7.1.

### 7.3 Wire parameters

Now that the wire material and the beam have been defined, it remains to define the wire speed and diameter. The diameter for PSI or HL-LHC is assumed to be 34  $\mu\text{m}$ , the same as for currently used wires. For the speed, at PSI, the speed chosen is 2.97  $\text{cm s}^{-1}$ , the speed now used for RRL. For HL-LHC, the speed is much higher, 1  $\text{m s}^{-1}$ . Because of beam size and LHC revolution time use of higher speed makes no sense, as not the full beam will be scanned. It must be noted that the wires could be used only to scan the beam halo, but this scenario is not considered here. See section "Wire parameters" in Table 7.1. For PSI and ADS cases, the initial temperature needs to be set to the temperature of the RF heating ( $\approx 1030 \text{ K}$ ). For HL-LHC the initial temperature is the ambient temperature, 300 K.

### 7.4 Simulations parameters

For the parameters related to the simulation, the number of steps is identical for all the cases, however, the resolution of the wire (the number of slices that cut the wire) is different between the PSI cases and the HL-LHC case because for the latter the beam is smaller so it is necessary to have smaller delimitations. This information is summarised in the section "Simulation parameters" of Table 7.1

	PSI Orbit 10	PSI Orbit 16	ADS	HL-LHC
<b>Beam parameters</b>				
Beam Energy	105.6 MeV	123 MeV	123 MeV	450 GeV (Beam at injection)
Stopping power	6.231 MeV cm <sup>2</sup> g <sup>-1</sup>	5.575 MeV cm <sup>2</sup> g <sup>-1</sup>	5.575 MeV cm <sup>2</sup> g <sup>-1</sup>	1.27 MeV cm <sup>2</sup> g <sup>-1</sup>
Beam current	1496 $\mu$ A	1496 $\mu$ A	5 mA	270 mA (25 % of nominal current [48])
$\sigma_H$	2.071 mm	1.633 mm	2.44 mm	625 $\mu$ m
$\sigma_V$	1.583 mm	1.502 mm	2.09 mm	625 $\mu$ m
<b>Wire parameters</b>				
Wire speed	2.97 cm s <sup>-1</sup>	2.97 cm s <sup>-1</sup>	2.97 cm s <sup>-1</sup>	1 m s <sup>-1</sup>
Wire material	CF or CNT	CF or CNT	CF or CNT	CF or CNT
Wire diameter	34 $\mu$ m	34 $\mu$ m	34 $\mu$ m	34 $\mu$ m
Wire initial temperature	1030 K	1030 K	1030 K	300 k
<b>Simulation parameters</b>				
Wire resolution	0.25 mm	0.25 mm	0.25 mm	0.10 mm
Time steps	10000	10000	10000	10000

Table 7.1: Beam, wire and simulation parameters for PSI, ADS and HL-LHC beams.

## 7.5 Results of the simulations and discussion

Thanks to the estimation of all these parameters it is possible to perform simulations with PyTT. As mentioned before, PyTT code can compute the maximum temperature (so, the thermal behaviour) and the wire signal. Both are compared for all the beam's conditions. Three materials are compared, the carbon fibre wire, the carbon nanotube wire with 1.0 g cm<sup>-3</sup> density, and the carbon nanotube wire with 0.2 g cm<sup>-3</sup> density.

### 7.5.1 Thermal behaviour

For the thermal behaviour, two different simulations are done for each material. For the first one, only the heating of the wire is taken into account in the heat equation (4.2). It is done to illustrate that, in the absence of cooling processes, the temperature does not depend on density. In the second simulation, radiative and thermionic cooling are also taken into account.

## PSI's Main Ring Cyclotron beams

Results of the thermal evolution simulations for PSI Main Ring Cyclotron beam are shown in Figures 7.3 and 7.4.

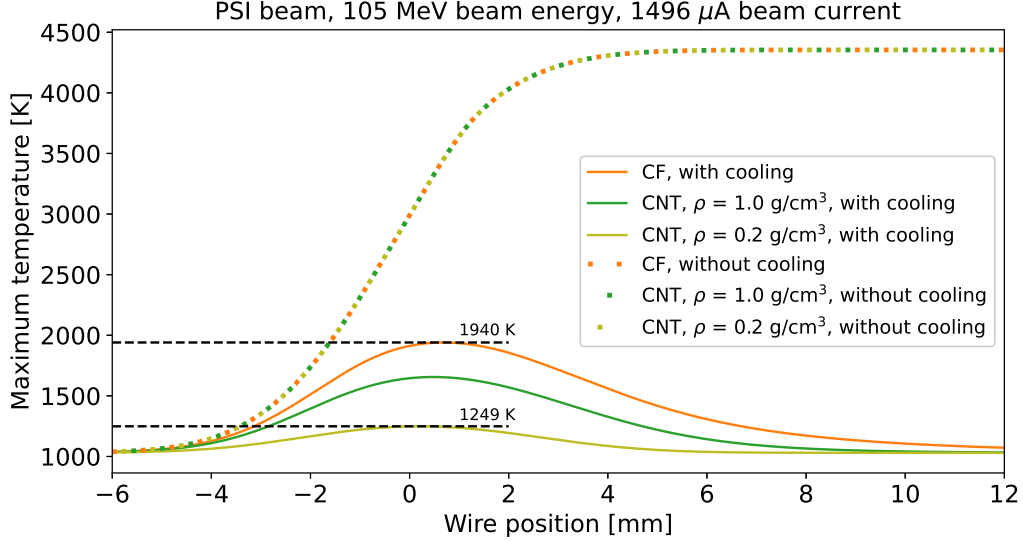


Figure 7.3: Thermal behaviour for PSI beam with 105 MeV beam energy and  $1496 \mu\text{A}$  beam current for CNT and CF. Dotted lines overlapping: only the heating process is simulated, solid lines: heating and cooling processes are simulated.

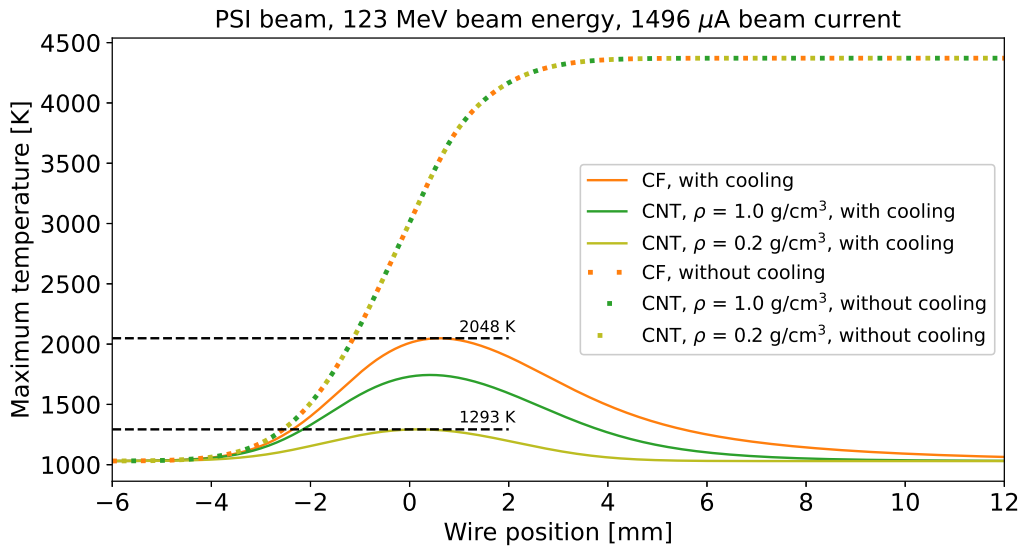


Figure 7.4: Thermal behaviour for PSI beam with 123 MeV beam energy and  $1496 \mu\text{A}$  beam current for CNT and CF. Dotted lines overlapping: only the heating process is simulated, solid lines: heating and cooling processes are simulated.

### ADS's cyclotron beam

Results of the thermal evolution simulations for ADS's cyclotron beam are presented in Figure 7.5

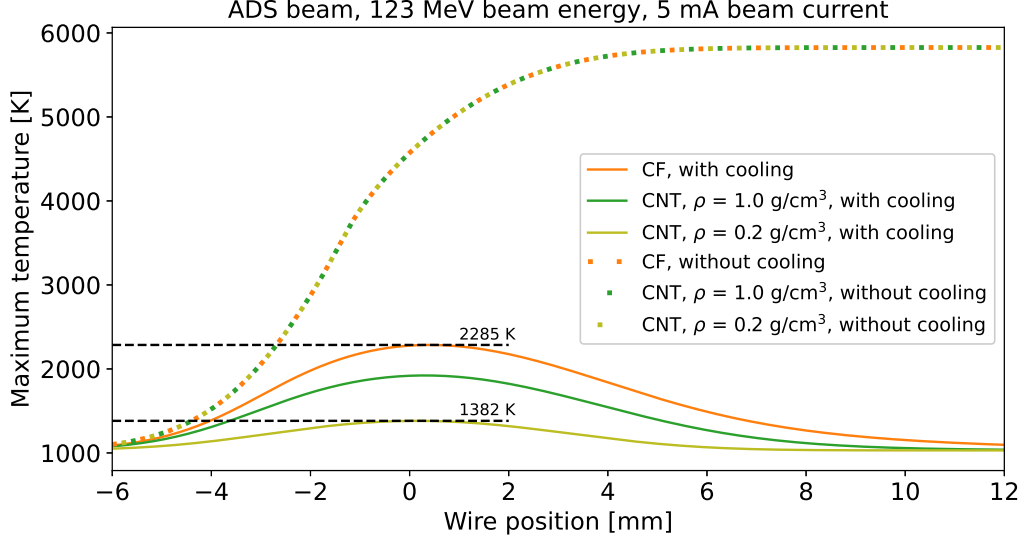


Figure 7.5: Thermal behaviour for ADS beam with 123 MeV beam energy and 5 mA beam current for CNT and CF. Dotted lines overlapping: only the heating process is simulated, solid lines: heating and cooling processes are simulated.

### HL-LHC's beam

Results of the thermal evolution simulations for the HL-LHC's beam are presented in Figure 7.6.

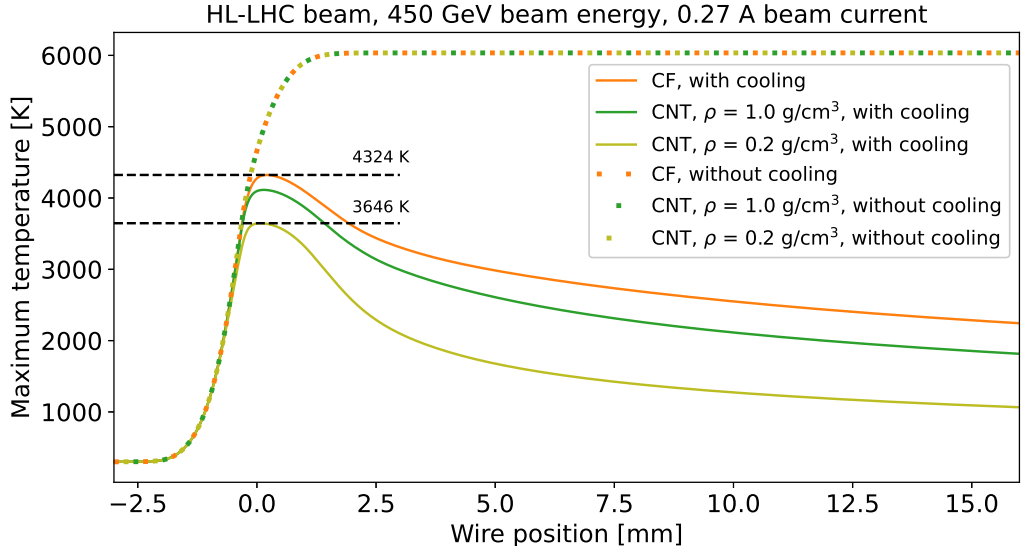


Figure 7.6: Thermal behaviour for HL-LHC beam with 450 GeV beam energy and 0.27 A beam current. Dotted lines overlapping: only the heating process is simulated, solid lines: heating and cooling processes are simulated.

## Discussion

In the first approximation, if only the beam heating is taken into account in the heat equation (4.2), the wire is heated very quickly. No matter what materials are used to make the wire, the temperature evolution is strictly the same. This is due to the fact that the beam heating  $\left(\frac{\partial T}{\partial t}\right)_{BH}$  (see equation (4.4)) does not depend on the density  $\rho$  of the material but only on the specific heat  $C_p(T)$ ,  $\frac{dE}{dx}$  and  $\Phi(x, y, t)$  being the same for the simulations with the same beam parameters.

However, wires are small objects and the cooling process is also very fast. When cooling processes are taken into account in the simulations (solid line in the Figures 7.3, 7.4, 7.5 and 7.6) the thermal behaviour is no longer the same. Indeed, cooling processes (see equation (4.5) for the radiative cooling  $\left(\frac{\partial T}{\partial t}\right)_{RC}$  and equation (4.7) for the thermionic cooling  $\left(\frac{\partial T}{\partial t}\right)_{TC}$ ) are inversely dependent on the density of the material. With smaller density, the maximum temperatures reached by the wire are smaller than the ones reached with bigger-density materials. For the HL-LHC case, the difference of temperature between CF and CNT with  $0.2 \text{ g cm}^{-3}$  is almost 700 K. The maximum temperature is 3646 K with  $0.2 \text{ g cm}^{-3}$  density CNT wire instead of 4324 K for the CF wire. As the sublimation point of carbon is around 3900 K (see Table 3.1),  $0.2 \text{ g cm}^{-3}$  density CNT could be used to scan 25 % of the beam at injection, unlike CF.

Therefore, assuming the same heat capacity of CF and CNT, temperature rises are the same for both materials but the cooling is faster for CNT wires because of the smaller amount of material.

For PSI and ADS beams, the temperature profile looks symmetric, the temperature comes back to the initial temperature which corresponds to the temperature of the RF heating, because of the very slow wire scanner movement. In the case of the HL-LHC, the cooling process is slow with respect to the wire speed.

The difference between the maximum temperature reached without the cooling processes and with the cooling processes is smaller for HL-LHC beams than for the cases with PSI and ADS beams. This is due to the speed of the wire which is much larger for HL-LHC wire scanner. With a  $1 \text{ m s}^{-1}$  speed, the cooling processes have less time to act than when the speed is only  $3 \text{ cm s}^{-1}$ . Then the effect of the heat capacity is more important.

### 7.5.2 Wire damage due to contamination

As written before, the contamination of the carbon nanotube can lead to damage when there are interactions between the beam and the wire as was the case in experiments from A. Mariet for his PhD Thesis [43]. The samples that he used for his experiment were contaminated with iron particles from the substrate used to grow nanotubes. Thanks to the Electron Microscopy and Diffraction group from PSI the samples of carbon nanotubes from H. Sugime [44] have been analysed with a X-ray spectrometer to determine what are the elements present in the samples. After looking at an overview, parts are looked at in more detail, like the end of the strand in Figure 7.7 where some particles can be distinguished from the carbon

nanotube. These particles are suspected to be iron from the substrate as in the case of CNT from [43]. By doing the X-ray spectroscopy in the selection area (yellow rectangle in Figure 7.7) it is possible to see that in fact, iron is not detected in this sample, which is positive (see the spectrum in Figure 7.8). However other elements have been detected, such as oxygen, that come from the environment, but also some peaks could be attributed to nickel, silicon and fluorine. A peak for aluminium is visible because this is the material of the sample holder. The important thing to note is that there are no metallic pieces in the samples.

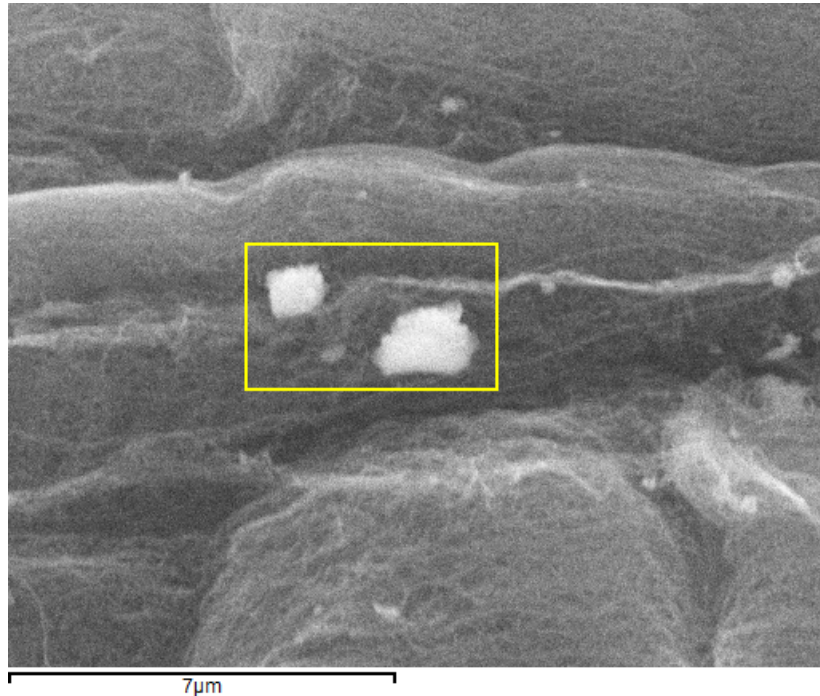


Figure 7.7: SEM image of the carbon nanotubes from [44]. The yellow rectangle corresponds to the selection used for the X-ray spectroscopy.

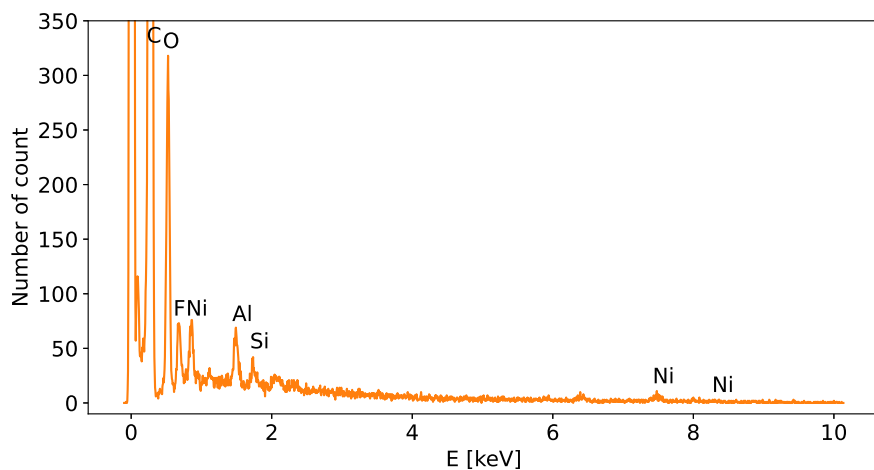


Figure 7.8: X-ray spectroscopy of the carbon nanotube from [44].

### 7.5.3 Wire signal

Unlike the simulations for thermal behaviour, for the wire signal only the cases with beam heating and cooling processes are shown. Studying the influence of the wire material on the wire signal makes it possible to determine what change this produces in the thermionic current, one of the major problems of wire scanners such as RRL. To compare and to distinguish the thermionic peak, simulations with only secondary emission current for carbon fibre wire are done.

#### PSI's Main Ring Cyclotron beams

The results for PSI's Main Ring Cyclotron are shown in Figures 7.9 and 7.10.

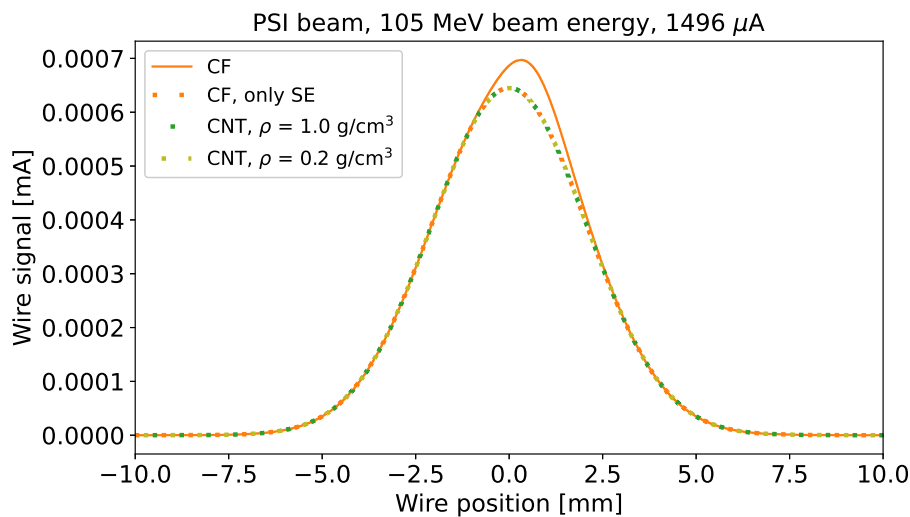


Figure 7.9: Wire signal for PSI beam with 105 MeV beam energy and 1496  $\mu\text{A}$  beam current for CNT and CF.

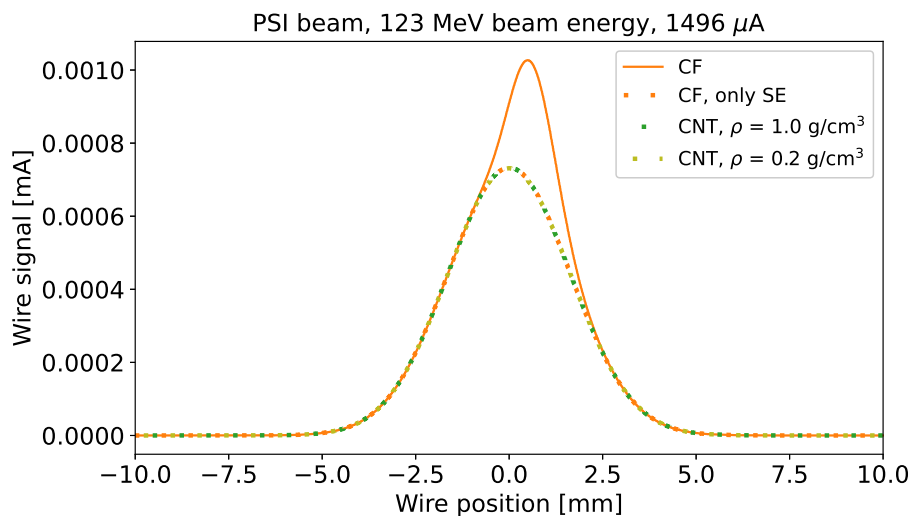


Figure 7.10: Wire signal for PSI beam with 123 MeV beam energy and 1496  $\mu\text{A}$  beam current for CNT and CF.

## ADS's cyclotron beam

Results for ADS's cyclotron beam are depicted in Figure 7.11.

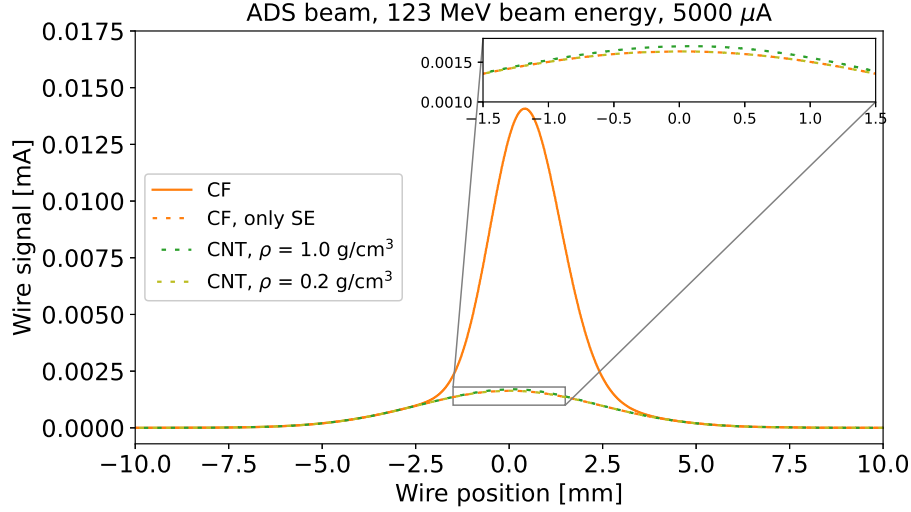


Figure 7.11: Wire signal for ADS beam with 123 MeV beam energy and 5000  $\mu\text{A}$  beam current for CNT and CF.

## HL-LHC beam

For the HL-LHC beam, results for the wire signal are represented in Figure 7.12.

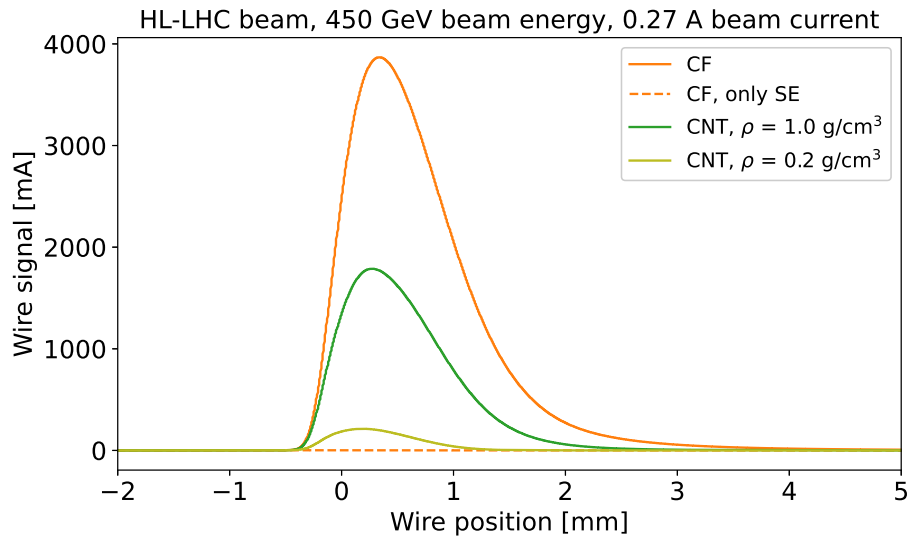


Figure 7.12: Thermal behaviour for HL-LHC beam with 450 GeV beam energy and 0.27 A beam current for CNT and CF.

## Discussion

As it is visible in Figures 7.9, and 7.10, the thermionic peak totally disappears when the wire is in carbon nanotubes for PSI cases. Indeed, the wire signals for CNTs are the same as for CF with only secondary electron emission. For the ADS case, with the largest density CNT, a very weak thermionic current remains (see Figure 7.11). This disappearance is due to the fact that the wire temperature is much lower for low-density materials than for carbon fibres, as shown in the previous Section. As the temperature is lower, the thermionic current, which depends on the temperature by a factor  $T^2 \exp\left(-\frac{\phi}{k_B T}\right)$ , is therefore much lower, or even non-existent. This preliminary result shows **great advantages presented by low-density materials in measurements done at PSI**. The use of carbon nanotube wires should completely neutralise thermionic emission without the need for any bias voltage, which, as shown in Chapter 5, is only partly effective.

For HL-LHC's beam, the thermionic peak is huge, for the three cases, even if it decreases with the density of the wire material. These results highlight a reason why the wire scanners used in accelerators with a high-energy beam are not based on the current generated in the wire. In fact, the thermal emissions are far too high, which is why detection of the secondary particles emitted is used.

# Chapter 8

## Conclusions and perspectives

The aim of this thesis was to determine what are the best solutions to suppress the thermionic emission current, a current that distorts the signal produced by the secondary electron emission.

The solution currently used in the case of the RRL probe is to apply a bias voltage to the wire. By observing the data measured by RRL, Chapter 5 showed that the bias voltage is only partly effective in suppressing thermionic emissions during the passage of the beam, whatever the voltage applied. In fact, a residual thermionic current of about 8% was observed in the measurements carried out by RRL in 2022 at different voltages. The beam potential would allow the thermionic electrons to escape, in the same way as the secondary emission electrons escape, and thus counter the effect of the bias voltage. We have to notice that the Main Ring cyclotron has long bunches with respect to the bunch spacing therefore, the presence of the beam has a large time fraction. In other machines with a smaller presence of the beam, applying a bias voltage should work better.

To study future possible solutions, the code PyTT is used. A benchmarking of this code with comparisons with experimental data is done. Measurements realized with RRL for 3 distinct cases have been compared with simulations with the same parameters. For cases without a thermionic peak or with a relatively small one, the code allowed us to correctly describe the wire signal, one must still note that the simulated secondary emission current is slightly bigger than the measured one. In the case with a high thermionic peak, PyTT has shown a discrepancy with measurements, the peak shape, in particular, its narrowness and its amplitude were not reproduced by the code. This could come from the high sensitivity of the code to certain temperature-dependent parameters like the emissivity and the work function, and some phenomena that are not simulated like the space charge production.

The first considered solution to the thermionic current issue is to use thinner targets. Simulations with PyTT showed that if the wire diameter is reduced to  $8 \mu\text{m}$  (the actual size is  $34 \mu\text{m}$ ), then the thermionic emission could be entirely suppressed, even for a beam current of  $2.4 \text{ mA}$ , which corresponds to the highest beam current reached by HIPA. The problems are that ultra-thin wires have less mechanical strength, and they are really difficult to handle. Also, if in the future the beam current increases, the diameter should be smaller than  $8 \mu\text{m}$ .

The other solution examined to remove thermionic emission is to change the

material of the wire. Simulations using several beams (actual PSI beams, estimation of future ADS beam, and future HL-LHC beam) have allowed us to confront carbon fibres with carbon nanotubes as wire scanner targets. This highlighted that the utilisation of carbon nanotube wires could decrease the thermionic emissions, and in the most extreme PSI beams could totally suppress them and therefore correct the observed deformation of the measured beam profile. These low-density materials could have a major role in beam instrumentation in the coming years as shown by the conclusions of a workshop on the subject [42].

The further exploration of the subject could include the following points:

- It could be interesting to run simulations of the energy deposition and secondary emission using Geant4 [49] a toolkit to simulate the passage of particles through matter. As it was written in Chapter 4, the  $\delta$ -electrons have not been taken into account in the stopping power calculation and may play a role in the thermal evolution.
- Simulations of the electric field around the wire and tracking of the escaping electrons in the presence of the bunch field could be very useful to see how escaping electrons are trapped by the bunch. This was attempted with the simulation code Virtual-IPM [31] but it was not conclusive.
- Taking data at low biases (between 2-5 eV) with RRL is necessary to understand the effect of the bias voltage on the measured profile and verify hypothesis made with the energy spectrum (see Section 4.3.1). It was not possible to do it during the period of this work because as explained before, no data were taken by RRL in 2023 due to the breakage of the wires.
- Mounting a carbon nanotube wire in RRL and producing beam profiles could be interesting to validate results found with simulations. If simulations and experiments are in agreement, that would say that no more bias voltage is needed for RRL.
- The space charge produced by the thermionic electrons can have an influence on the thermionic emission and needs to be determined to try to explain the discrepancy between the simulations done with PyTT and the measurements done with RRL when the thermionic current is high.
- The determination by experimentation in labs of the work function of carbon fibre and nanotube wires, as well as emissivity, especially at high temperature.

# Bibliography

- [1] P. Fork, “Lecture Notes on Beam Instrumentation and Diagnostics,” in *Joint University Accelerator School*, Jan. 2023. [Online]. Available: [https://indico.cern.ch/event/1214547/contributions/5109013/attachments/2596536/4482436/juas\\_script.pdf](https://indico.cern.ch/event/1214547/contributions/5109013/attachments/2596536/4482436/juas_script.pdf) (visited on 07/07/2023).
- [2] M. Gasior, R. Jones, T. Lefevre, H. Schmickler, and K. Wittenburg, “Introduction to Beam Instrumentation and Diagnostics,” en, *CERN Yellow Report CERN-2014-009, pp.23-60*, Jan. 2016. DOI: [10.5170/CERN-2014-009.23](https://doi.org/10.5170/CERN-2014-009.23). arXiv: [1601.04907 \[physics.acc-ph\]](https://arxiv.org/abs/1601.04907).
- [3] Paul Scherrer Institute, “The Paul Scherrer Institute in brief,” [Online]. Available: <https://www.psi.ch/en/about/psi-in-brief> (visited on 06/23/2023).
- [4] Paul Scherrer Institute, “The PSI proton accelerator,” [Online]. Available: <https://www.psi.ch/en/media/the-psi-proton-accelerator> (visited on 06/30/2023).
- [5] M. Sapinski, R. Dölling, and M. Rohrer, “Commissioning of the Renewed Long Radial Probe in PSI Ring Cyclotron,” en, *Proceedings of the 11th International Beam Instrumentation Conference, Poland*, vol. IBIC2022, pp. 76–79, 2022. DOI: [10.18429/JACOW-IBIC2022-MOP19](https://doi.org/10.18429/JACOW-IBIC2022-MOP19).
- [6] O. W. Richardson, “Electron Emission from Metals as a Function of Temperature,” *Physical Review*, vol. 23, no. 2, pp. 153–155, Feb. 1924. DOI: [10.1103/physrev.23.153](https://doi.org/10.1103/physrev.23.153).
- [7] A. Navarro, “PyTT GitHub page,” 2022. [Online]. Available: <https://github.com/navarrof/PyTT> (visited on 07/08/2023).
- [8] Paul Scherrer Institute, “Center for Proton Therapy CPT,” [Online]. Available: <https://www.psi.ch/en/protontherapy> (visited on 07/24/2023).
- [9] Paul Scherrer Institute, “Swiss Light Source - SLS,” [Online]. Available: <https://www.psi.ch/de/sls> (visited on 07/24/2023).
- [10] Paul Scherrer Institute, “The SwissFEL X-ray free-electron laser,” [Online]. Available: <https://www.psi.ch/en/media/the-swissfel-x-ray-free-electron-laser> (visited on 07/25/2023).
- [11] J. Grillenberger, C. Baumgarten, and M. Seidel, “The High Intensity Proton Accelerator Facility,” *SciPost Physics Proceedings*, no. 5, Sep. 2021. DOI: [10.21468/scipostphysproc.5.002](https://doi.org/10.21468/scipostphysproc.5.002).

- [12] Paul Scherrer Institute, “A reliable type from the 1980s,” [Online]. Available: <https://www.psi.ch/en/media/our-research/a-reliable-type-from-the-1980s> (visited on 06/30/2023).
- [13] Paul Scherrer Institute, “Injector 2: A pre-accelerator for protons,” [Online]. Available: <https://www.psi.ch/en/media/our-research/injector-2-a-pre-accelerator-for-protons> (visited on 06/30/2023).
- [14] Paul Scherrer Institute, “S $\mu$ S: Swiss Muon Source,” [Online]. Available: <https://www.psi.ch/en/smus> (visited on 06/30/2023).
- [15] Paul Scherrer Institute, “SINQ: The Swiss Spallation Neutron Source,” [Online]. Available: <https://www.psi.ch/en/media/our-research/injector-2-a-pre-accelerator-for-protons> (visited on 06/30/2023).
- [16] B. Lauss and B. Blau, “UCN, the ultracold neutron source – neutrons for particle physics,” *Review of Particle Physics at PSI*, Apr. 2021. DOI: [10.48550/ARXIV.2104.02457](https://doi.org/10.48550/ARXIV.2104.02457) [nucl-ex]. arXiv: [2104.02457](https://arxiv.org/abs/2104.02457) [nucl-ex].
- [17] J. Rumble, *CRC Handbook of Chemistry and Physics*, 104th, CRC Press, Ed. Boca Raton, Florida: Taylor Francis Group, 2023, ISBN: 9781032425207.
- [18] A. Navarro, “Understanding Secondary Emission Processes and Beam Matter interactions for Optimization of Diagnostic Wire Grid System in Particle Accelerators,” PhD Thesis, Universitat Politècnica de Catalunya, BarcelonaTech, Barcelona, 2022. [Online]. Available: <https://cds.cern.ch/record/2858279> (visited on 08/08/2023).
- [19] R. L. Workman *et al.*, “34. Passage of Particles Through Matter, Review of Particle Physics,” *Particle Data Group PTEP*, vol. 2022, p. 083C01, 2022. DOI: [10.1093/ptep/ptac097](https://doi.org/10.1093/ptep/ptac097).
- [20] J. Bosser, J. Camas, L. Evanss, *et al.*, “The Micron Wire scanner at the SPS,” *CERN SPS/86-26 (MS)*, 1986. [Online]. Available: [https://accelconf.web.cern.ch/p87/PDF/PAC1987\\_0783.PDF](https://accelconf.web.cern.ch/p87/PDF/PAC1987_0783.PDF) (visited on 08/08/2023).
- [21] M. Sapinski, “Model of Carbon Wire Heating in Accelerator Beam,” *CERN-AB-2008-030*, 2008. [Online]. Available: <https://cds.cern.ch/record/1123363?ln=fr> (visited on 08/08/2023).
- [22] S. Seltzer, *Stopping-Powers and Range Tables for Electrons, Protons, and Helium Ions, NIST Standard Reference Database 124*, en, 1993. DOI: [10.18434/T4NC7P](https://doi.org/10.18434/T4NC7P).
- [23] E. J. Sternglass, “Theory of Secondary Electron Emission by High-Speed Ions,” *Physical Review*, vol. 108, no. 1, pp. 1–12, Oct. 1957. DOI: [10.1103/physrev.108.1](https://doi.org/10.1103/physrev.108.1).
- [24] D. Hasselkamp, S. Hippler, and A. Scharmann, “Ion-induced secondary electron spectra from clean metal surfaces,” *Nuclear Instruments and Methods in Physics Research Section B: Beam Interactions with Materials and Atoms*, vol. 18, no. 1-6, pp. 561–565, 1986. DOI: [10.1016/s0168-583x\(86\)80088-x](https://doi.org/10.1016/s0168-583x(86)80088-x).

- [25] M. S. Chung and T. E. Everhart, “Simple calculation of energy distribution of low-energy secondary electrons emitted from metals under electron bombardment,” *Journal of Applied Physics*, vol. 45, no. 2, pp. 707–709, Feb. 1974. DOI: [10.1063/1.1663306](https://doi.org/10.1063/1.1663306).
- [26] W. Schmickler and E. Santos, “A few basic concepts,” in *Interfacial Electrochemistry*, Springer Berlin Heidelberg, 2010, pp. 29–37. DOI: [10.1007/978-3-642-04937-8\\_4](https://doi.org/10.1007/978-3-642-04937-8_4).
- [27] K. Uppireddi, T. L. Westover, T. S. Fisher, B. R. Weiner, and G. Morell, “Thermionic emission energy distribution from nanocrystalline diamond films for direct thermal-electrical energy conversion applications,” *Journal of Applied Physics*, vol. 106, no. 4, p. 043716, Aug. 2009. DOI: [10.1063/1.3204667](https://doi.org/10.1063/1.3204667).
- [28] M. Sapinski and M. Boucard, “Dealing with Thermionic Emission in Wire Scanners based on Secondary Electron Emission,” in *Proc. IPAC’23*, (Venezia), ser. IPAC’23 - 14th International Particle Accelerator Conference - Venezia, JACoW Publishing, Geneva, Switzerland, May 2023, pp. 4769–4772, ISBN: 978-3-95450-231-8. DOI: [doi:10.18429/jacow-ipac2023-thpl150](https://doi.org/10.18429/jacow-ipac2023-thpl150).
- [29] “Jupyter notebook,” [Online]. Available: <https://jupyter.org/> (visited on 07/08/2023).
- [30] R. Dölling, “Bunch-shape Measurements at PSI’s High-power Cyclotrons and Proton Beam-line,” in *Proceedings of Cyclotrons 2013, Vancouver, Canada*, ser. Cyclotron subsystem, Diagnostics, 2013, pp. 257–261. [Online]. Available: <http://accelconf.web.cern.ch/CYCLOTRONS2013/papers/tu3pb01.pdf> (visited on 08/07/2023).
- [31] D. Vilsmeier, “Virtual-IPM Python Package Index,” [Online]. Available: <https://pypi.org/project/virtual-ipm/> (visited on 06/30/2023).
- [32] A. Abouelenain, “Beam wire scanner at CERN: Simulation of behavior of carbon nanotube wires with protons at high energies,” M.S. thesis, Université de Franche-Comté, Besançon, 2023.
- [33] C. B. Do, “The Multivariate Gaussian Distribution,” 2008. [Online]. Available: <https://cs229.stanford.edu/section/gaussians.pdf> (visited on 07/08/2023).
- [34] C. Baumgarten and H.Zhang, “Private communication.”
- [35] Y. S. Touloukian and E. H. Buyco, “Thermophysical properties of matter - the TPRC data series. Volume 5. Specific heat - nonmetallic solids. data book,” Purdue Univ., Lafayette, IN (United States). Thermophysical and Electronic Properties Information Center, Tech. Rep., 1970. [Online]. Available: <https://www.osti.gov/biblio/5303501> (visited on 07/08/2023).
- [36] X. Li and W. Strieder, “Emissivity of high-temperature fiber composites,” *Industrial & Engineering Chemistry Research*, vol. 48, no. 4, pp. 2236–2244, Jan. 2009. DOI: [10.1021/ie8008583](https://doi.org/10.1021/ie8008583).
- [37] M. Avraham, G. Golan, and Y. Nemirovsky, “Novel grey body for accurate radiometric measurements,” *Micromachines*, vol. 14, no. 5, p. 974, Apr. 2023. DOI: [10.3390/mi14050974](https://doi.org/10.3390/mi14050974).

- [38] A. Kiejna, K. F. Wojciechowski, and J. Zebrowksi, “The temperature dependence of metal work functions,” *Journal of Physics F: Metal Physics*, vol. 9, no. 7, pp. 1361–1366, Jul. 1979. DOI: [10.1088/0305-4608/9/7/016](https://doi.org/10.1088/0305-4608/9/7/016).
- [39] R. Rahemi and D. Li, “Variation in electron work function with temperature and its effect on the Young’s modulus of metals,” *Scripta Materialia*, vol. 99, pp. 41–44, Apr. 2015. DOI: [10.1016/j.scriptamat.2014.11.022](https://doi.org/10.1016/j.scriptamat.2014.11.022).
- [40] M. Sapinski, B. Dehning, A. Guerrero, T. Kroyer, and M. Meyer, “Carbon Fiber Damage in Particle Beam,” in *46th ICFA Advanced Beam Dynamics Workshop on High- Intensity and High-Brightness Hadron Beams, Morschach, Switzerland*, 2010, pp. 231–234. [Online]. Available: <https://accelconf.web.cern.ch/hb2010/papers/mopd63.pdf> (visited on 08/08/2023).
- [41] M. Sapinski, “About the damage mechanisms of thin targets exposed to high-power particle beams,” in *Proc. IPAC’23*, (Venezia), ser. IPAC’23 - 14th International Particle Accelerator Conference, JACoW Publishing, Geneva, Switzerland, May 2023, pp. 4773–4776, ISBN: 978-3-95450-231-8. DOI: [doi:10.18429/jacow-ipac2023-thpl151](https://doi.org/10.18429/jacow-ipac2023-thpl151). [Online]. Available: <https://indico.jacow.org/event/41/contributions/2499>.
- [42] “Low-density materials for beam instrumentation, indico webpage,” 2023. [Online]. Available: <https://indico.cern.ch/event/1275649/> (visited on 06/30/2023).
- [43] A. Mariet, “Study of the effects of copper coating and proton irradiation at 440 GeV on the mechanical properties of carbon nanotube wires for particle beam instrumentation at CERN. Etude des effets du cuivrage et de l’irradiation par proton à 440 GeV sur les propriétés mécaniques de fils en nanotubes de carbone pour l’instrumentation des faisceaux au CERN,” Presented 03 May 2023, PhD Thesis, Université de Franche-Comté, Besançon, 2023. [Online]. Available: <http://cds.cern.ch/record/2860710> (visited on 08/08/2023).
- [44] H. Sugime, T. Sato, R. Nakagawa, T. Hayashi, Y. Inoue, and S. Noda, “Ultra-long carbon nanotube forest via in situ supplements of iron and aluminum vapor sources,” *Carbon*, vol. 172, pp. 772–780, Feb. 2021. DOI: [10.1016/j.carbon.2020.10.066](https://doi.org/10.1016/j.carbon.2020.10.066).
- [45] H. Zhu, C. Masarapu, J. Wei, K. Wang, D. Wu, and B. Wei, “Temperature dependence of field emission of single-walled carbon nanotube thin films,” *Physica E: Low-dimensional Systems and Nanostructures*, vol. 41, no. 7, pp. 1277–1280, Jun. 2009. DOI: [10.1016/j.physe.2009.02.010](https://doi.org/10.1016/j.physe.2009.02.010).
- [46] World Nuclear Association, “Accelerator-driven Nuclear Energy,” [Online]. Available: <https://world-nuclear.org/information-library/current-and-future-generation/accelerator-driven-nuclear-energy.aspx> (visited on 07/08/2023).
- [47] “High Luminosity LHC Project,” [Online]. Available: <https://hilumilhc.web.cern.ch/> (visited on 08/08/2023).

- [48] I. Bejar, O. Brüning, P. Fessia, L. Rossi, R. Tomas, and M. Zerlauth, “The HL-LHC Machine,” in *The High Luminosity Large Hadron Collider*, WORLD SCIENTIFIC, Sep. 2015, pp. 31–44. DOI: [10.1142/9789814675475\\_0003](https://doi.org/10.1142/9789814675475_0003).
- [49] S. Agostinelli, J. Allison, K. Amako, *et al.*, “Geant4—a simulation toolkit,” *Nuclear Instruments and Methods in Physics Research Section A: Accelerators, Spectrometers, Detectors and Associated Equipment*, vol. 506, no. 3, pp. 250–303, Jul. 2003. DOI: [10.1016/s0168-9002\(03\)01368-8](https://doi.org/10.1016/s0168-9002(03)01368-8).